Review

Emerging Trends in Thermo-Optic and Electro-Optic Materials for Tunable Photonic Devices

Muhammad A. Butt *

Posted Date: 13 May 2025

doi: 10.20944/preprints202505.0911.v1

Keywords: reconfigurable photonic devices; thermo-optic; electro-optic; Pockels effect; Kerr effect

 doi:10.20944/preprints202505.0911.v1

Review

Emerging Trends in Thermo-Optic and Electro-Optic Materials for Tunable Photonic Devices

Muhammad A. Butt

Warsaw University of Technology, Institute of Microelectronics and Optoelectronics, Koszykowa 75, 00-662, Warsaw, Poland; ali.butt@pw.edu.pl

Abstract: Tunable photonic devices are increasingly pivotal in modern optical systems, enabling dynamic control over light propagation, modulation, and filtering. This review systematically explores two prominent classes of materials, thermo-optic and electro-optic, for their roles in such tunable devices. Thermo-optic materials utilize refractive index changes induced by temperature variations, offering simple implementation and broad material compatibility, although often at the cost of slower response times. In contrast, electro-optic materials, particularly those exhibiting the Pockels and Kerr effects, enable rapid and precise refractive index modulation under electric fields, making them suitable for high-speed applications. The paper discusses the underlying physical mechanisms, material properties, and typical figures of merit for each category, alongside recent advancements in organic, polymeric, and inorganic systems. Furthermore, integrated photonic platforms and emerging hybrid material systems are highlighted for their potential to enhance performance and scalability. By evaluating the tradeoffs in speed, power consumption, and integration complexity, this review identifies key trends and future directions for deploying thermo-optic and electro-optic materials in the next generation tunable photonic devices.

Keywords: reconfigurable photonic devices; thermo-optic; electro-optic; Pockels effect; Kerr effect

1. Introduction

Photonic devices, which manipulate and control the propagation of light, are central to a wide range of modern technologies including optical communications, sensing systems, imaging platforms, and emerging fields such as quantum information processing[1–4]. As these technologies evolve, there is a growing need for optical components that can dynamically adjust their behavior in real time[5–8]. Devices with fixed optical properties are often insufficient for systems that require flexibility and adaptability. This increasing demand has led to the development of tunable photonic devices, which can modify their optical characteristics such as refractive index or transmission spectrum in response to external stimuli[9–11]. The ability to reconfigure photonic devices on demand is essential for enabling multifunctional operation, enhancing system performance, and supporting scalable architectures in advanced applications like optical networks, beam steering, and signal modulation[12,13].

Among the various mechanisms that enable tunability in photonic systems, the thermo-optic (TO)[14,15] and electro-optic (EO)[13,16] effects are particularly significant due to their strong influence on optical behavior and their compatibility with integrated device platforms. The TO effect refers to the variation of a material's refractive index as a function of temperature, typically described by the TO coefficient[17]. This effect can be harnessed through localized heating techniques, allowing controlled changes in optical properties over time. The EO effect, on the other hand, involves a change in refractive index in response to an applied electric field. This phenomenon can occur through either the linear Pockels effect or the nonlinear Kerr effect, depending on the symmetry and electronic structure of the material[18–20]. EO modulation is often much faster than TO tuning and is widely used in high-speed applications such as optical switches and modulators[21,22].

 doi:10.20944/preprints202505.0911.v1

The effectiveness of tunable photonic devices is closely tied to the properties of the materials used[23–27]. An ideal material for TO[28–30] or EO tuning[31–33] should exhibit a large change in refractive index with minimal energy input, low optical absorption, thermal and chemical stability, and compatibility with fabrication processes used in photonic integration. For instance, silicon (Si) is a leading platform in integrated photonics due to its well-established manufacturing infrastructure and significant TO response[34–36]. However, Si lacks a linear EO effect due to its centrosymmetric crystal structure, limiting its use in high-speed modulation applications. This challenge has motivated the integration of EO active materials such as lithium niobate (LN), barium titanate (BTO), and organic polymers with Si to combine the benefits of both platforms[37,38]. In recent years, researchers have also begun exploring two-dimensional materials and hybrid perovskites for their promising optical properties and potential for scalable integration[17,39–41].

This review presents an in-depth analysis of materials employed in tunable photonic devices that leverage TO and EO effects. It begins by elucidating the physical principles underpinning these phenomena and continues with a thorough evaluation of various material platforms, including conventional semiconductors, ferroelectric oxides, polymers, and emerging materials such as graphene, chalcogenides, and transparent conductive oxides. Each material is discussed concerning its tunability, compatibility with photonic integration, and performance trade-offs in specific applications. The review further explores recent advancements in material engineering techniques, such as nanostructuring, doping, and heterostructure fabrication, that have improved optical tunability and broadened functional capabilities. The primary objective of this work is to deliver a comprehensive and critical overview of the current and emerging materials landscape for tunable photonics, identifying both the present capabilities and the key challenges that must be addressed to enhance device performance and integration for future photonic systems.

2. Fundamentals of TO and EO Effects

Tunable photonic devices depend critically on materials whose optical properties can be dynamically altered[27]. Among the most effective mechanisms for such modulation are the TO and EO effects[13,15]. These phenomena allow real-time control of key optical parameters such as refractive index and absorption, which in turn enables dynamic tuning of wavelength, phase, intensity, and polarization in integrated photonic circuits[42,43].

2.1. TO Effect in Photonic Tuning

The TO effect refers to the change in a material's refractive index due to temperature variation[30]. This relationship is quantified by the thermo-optic coefficient (TOC), represented mathematically as dn/dT. The TO effect is especially attractive for tunable photonic devices due to its broadband nature and compatibility with a wide range of materials[44]. In practical implementations, localized temperature control using integrated micro-heaters is employed to modulate the refractive index of photonic waveguides. This enables functionalities such as phase tuning, wavelength adjustment, and the detuning of optical resonators. Si photonics benefits significantly from this mechanism, with Si exhibiting a TOC of approximately 1.86×10^{-4} K^{-1}[45]. Although the response time of TO tuning is relatively slow, typically ranging from microseconds to milliseconds, it is widely used due to its design simplicity and low optical insertion loss. Beyond Si, materials such as polymers[30,46] and chalcogenide glasses[47,48] exhibit higher TOCs, making them suitable for more compact and power-efficient devices. Two-dimensional materials, including graphene oxide, are also gaining attention for their strong TO response and integration flexibility in photonic platforms[29,49].

Antimony sulfide (Sb_2S_3), a phase change material (PCM) with a wide bandgap, has been identified as a promising candidate for NIR tunable photonics due to its broadband optical transparency extending from the visible to the NIR spectrum[50]. Its suitability for integrated photonic applications has been explored through experimental analysis and device integration. Ilie et al. incorporated Sb_2S_3 onto a silicon nitride (SiN) photonic platform using a microring resonator (MRR) to investigate its thermally induced optical modulation capabilities[51]. Figure 1 (a) and (b)

 doi:10.20944/preprints202505.0911.v1

display SEM images of a variation of the MRR, along with a close-up view of the PCM deposited on the arc section. Figure 1 (c) presents a schematic of the SiNx RR, including a cross-sectional view that illustrates the fundamental TE optical mode. The thermo-optical behavior of Sb_2S_3 in the C-band was explored, focusing on its impact on high-density photonic applications. The temperature dependence of the RR resonance was studied between 20°C and 60°C using a Peltier stage, with measurements taken after 30 minutes of stabilization at each temperature. The temperature sensitivity of the bare SiNx RR's resonance wavelength increased from 10.8 pm/°C before annealing to 18.0 pm/°C after annealing (red and green lines in Figure 1 (d)). For the amorphous Sb_2S_3 state, the shift was 12.8 pm/°C, while the crystalline state exhibited a shift of 19.6 pm/°C. Despite changes in the thermo-optical properties of the ZnS-SiO_2 cladding after annealing, the optical losses remain comparable to those of air-cladded devices[51].

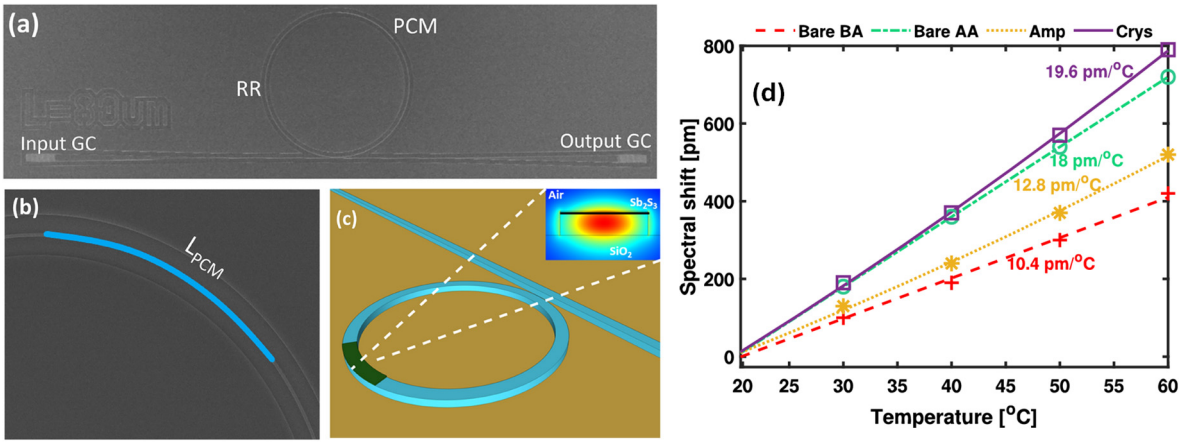

Figure 1. (a) SEM image of an MRR with a PCM layer on top, (b) Enlarged view of the PCM region, highlighted in blue, (c) Schematic of a SiNx microring partially coated with Sb_2S_3, with an inset showing the cross-section and TE mode profile, (d) Transmission spectra of the MRR measured at various temperatures for four configurations: (a) SiN RR without PCM, before annealing, (b) Same RR after annealing, (c) RR with Sb_2S_3 in the amorphous state, (d) RR with Sb_2S_3 in the crystalline state, with all spectra centered near 1550 nm[51].

Phase transitions between the amorphous and crystalline states of the material were utilized to achieve dynamic tuning of the resonator response, with extinction ratios reaching up to 18 dB in the C-band. TOCs were extracted for both states, measured at approximately 3.4×10^{-4} K^{-1} for the amorphous phase and 0.1×10^{-4} K^{-1} for the crystalline phase, reflecting a significant refractive index contrast. Additionally, permanent spectral trimming of the device was demonstrated through bidirectional tuning enabled by continuous-wave (CW) laser exposure in the range of -5.9 to 5.1 dBm. This process resulted in effective refractive index (n_{eff}) modulation from $+5.23 \times 10^{-5}$ to -1.20×10^{-4}. These findings confirmed the feasibility of using Sb_2S_3 for both reconfigurable and non-volatile photonic functionality. Potential applications include optically programmable memory, tunable synaptic elements for neuromorphic systems, and dense optical switching architectures within multilayer PECVD-based photonic integrated circuits (PICs) [51].

2.2. EO Effect in Photonic Tuning

The EO effect involves the modification of a material's refractive index in response to an externally applied electric field[33]. This effect provides a high-speed and energy-efficient tuning mechanism that is essential for advanced photonic systems. Two main types of EO effects are typically utilized in tunable photonic devices.

The Pockels effect, also known as the linear EO effect, occurs in non-centrosymmetric crystals such as LN[52] and BTO [53]. In these materials, the refractive index changes linearly with the applied electric field. The Pockels effect enables fast modulation speeds, with response times in the gigahertz range, and is commonly employed in modulators, tunable filters, and phase shifters. LN modulators

 doi:10.20944/preprints202505.0911.v1

are well-established in optical communications due to their high performance and reliability[54]. The Kerr effect, or the quadratic EO effect, is present in all materials and causes a refractive index to change that is proportional to the square of the applied electric field[55]. While generally weaker than the Pockels effect, the Kerr effect is useful in nonlinear optics and specific high-field applications[56].

Electro-absorption effects are another category of EO modulation, involving electric-field-induced changes in the material's absorption properties[57]. The Franz Keldysh effect in bulk semiconductors and the quantum confined Stark effect in quantum wells are two examples widely used in electro-absorption modulators[58,59]. These devices are particularly valuable in compact, high-speed optical interconnects based on III-V semiconductors. Emerging materials such as indium tin oxide (ITO)[60] and transparent conducting oxides (TCOs)[61,62] offer significant EO tunability. These materials support strong field-induced changes in permittivity and are being explored for integration into nanoscale and hybrid Si plasmonic devices, enabling high-performance modulation with a minimal footprint.

Two-dimensional materials like transition metal dichalcogenides (TMDs) and graphene have shown impressive optical responses to external stimuli, but challenges remain in achieving efficient modulation in the short-wave infrared (SWIR) region. Maintaining precise phase control and minimizing signal loss within a compact form factor is particularly difficult. Dushaq et al. investigated the electro-refractive behavior of multilayer $CuCrP_2S_6$ (CCPS) in the near-infrared wavelength range[33]. By embedding CCPS into Si photonic MRRs, light-matter interaction was enhanced, allowing for improved sensitivity to phase and absorption changes (Figure 2 (a)). Application of an electric field enabled the tuning of the n_{eff} by about 2.8×10^{-3} RIU, with minimal impact on extinction ratios and resonance linewidth. The devices also display low optical loss and high modulation efficiency of 0.25 V·cm, with a consistent blue shift in resonance wavelengths regardless of the voltage polarity.

Figure 2 (b) illustrates the redistribution of Cu ions in the CCPS/Si heterostructure under an electric field, altering both copper ion concentration and electrical conductivity. The soft Cu–S bond allows Cu ion movement within and across the van der Waals gap, enabling optical tuning controlled by voltage. Figure 2 (c) shows the transmission spectra of the Si/CCPS chip at varying laser input powers (0.66 mW to 11.2 mW) with a 0 V bias, revealing no significant resonance peak shifts, indicating no thermal dissipation. Measurements were limited to 11.2 mW to prevent power variations from affecting results. Figure 2 (d) presents the transmission spectra at bias voltages of 0 V and 7 V for TE polarization. With a constant 7 V bias, a consistent blue shift in resonance wavelengths is observed, indicating electro-optical modulation. The application of bias does not affect extinction ratios or linewidths, suggesting Cu ion migration does not influence the imaginary refractive index. Figure 2 (e) shows the change in n_{eff} as a function of polling time at 7 V, with a tuning efficiency of −8.3 pm/V. The n_{eff} can be tuned by 2.8×10^{-3} RIU, and the half-wave voltage-length product is estimated to be 0.25 ± 0.07 V·cm. Pre-poling of the CCPS material accelerates ion migration, like behaviors observed in ferroelectric PZT materials. Distinct differences in EO tuning are observed between TE and TM modes, indicating a polarization-dependent response. This characteristic expands the potential applications for light manipulation. The combination of optoelectronic and ionotronic properties in two-terminal CCPS devices offers significant promise for a wide range of applications, including optical switching, phased arrays, environmental sensing, optical imaging, and neuromorphic systems such as light-sensitive artificial synapses[33].

 doi:10.20944/preprints202505.0911.v1

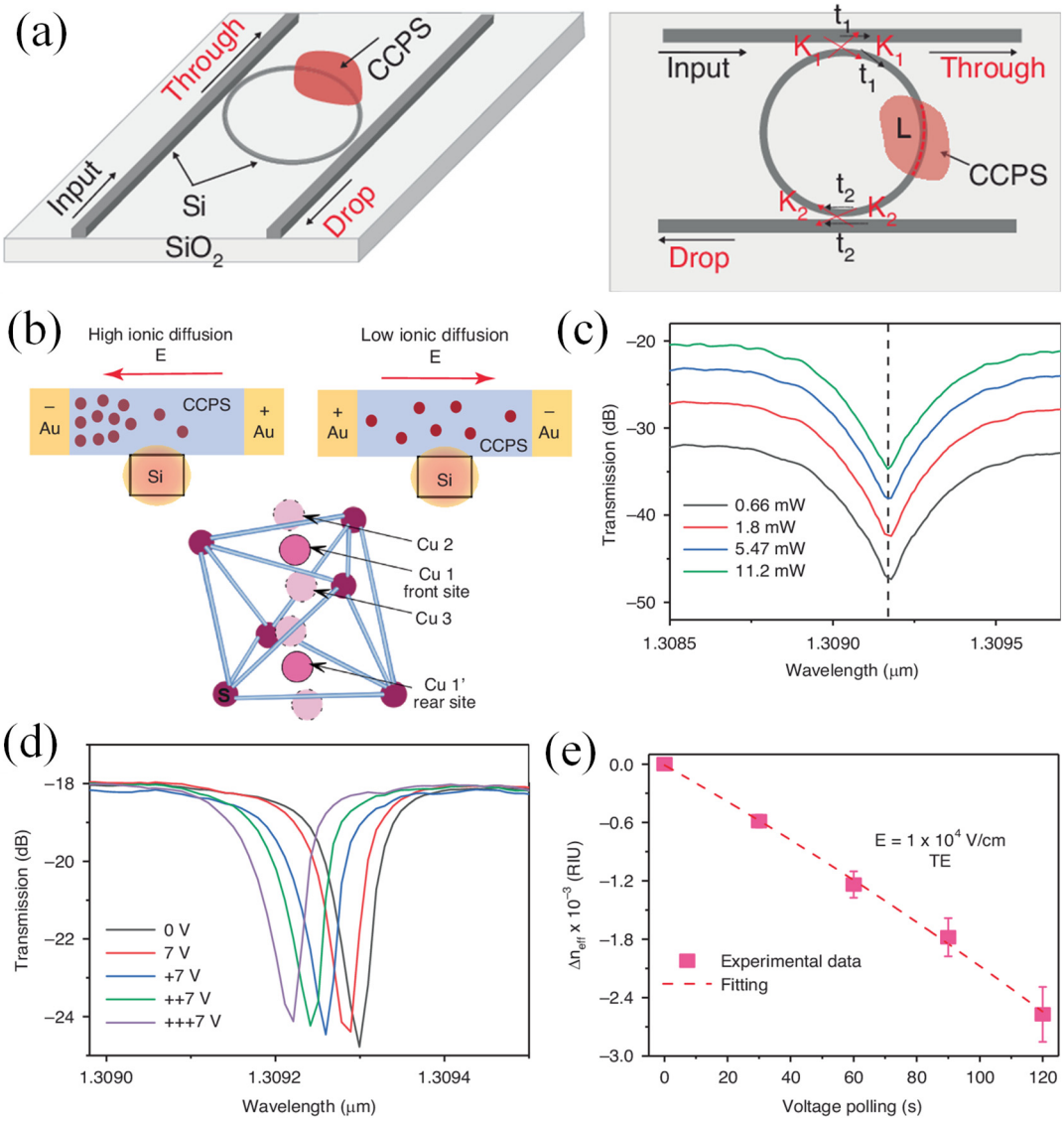

Figure 2. (a) 3D and cross-sectional views of the Si-MRR design incorporating CCPS, (b) A diagram illustrating the redistribution of copper ions within the CCPS/Si heterostructure when an electric field is applied, highlighting the movement of copper ions inside the sulfur cage, (c) Transmission spectra of the MRR measured at different input optical powers, (d) Transmission spectra of the MRR at a fixed voltage of 7 V over increasing polling times, (e) Change in the effective refractive index as a function of polling time, with an applied electric field of 1×10^4 V/cm [33].

3. Key Materials for TO Applications

TO tunable photonic devices play a vital role in modern optical systems, offering a reliable and power-efficient means of controlling light without requiring mechanical movement or complex electronic modulation. Key components such as switches[63], modulators[64], filters[65], and phase shifters[66,67] have been developed using TO principles, particularly on platforms like Si and LN, where strong TOCs enable efficient tuning. Their significance lies in their ability to provide compact, low-cost, and complementary metal-oxide semiconductor (CMOS)-compatible solutions for dynamic optical signal processing, wavelength routing, and reconfigurable photonic networks, making them essential building blocks in applications ranging from data centers and telecommunications to quantum photonics and lab-on-chip systems[30].

Key materials used in TO applications are chosen for their strong temperature-dependent refractive index, optical transparency, thermal stability, and compatibility with photonic integration (Table 1). Si is a widely adopted material due to its high TOC, efficient light confinement, and

 doi:10.20944/preprints202505.0911.v1

compatibility with standard CMOS fabrication processes[64,68]. Polymers are also frequently used because of their customizable properties and significant thermal response[69]. Silica, while having a lower TOC, is valued for its low optical loss and excellent thermal and chemical stability[70,71]. Other advanced materials include chalcogenide glasses, known for their high refractive index modulation[47], and PCMs such as germanium antimony telluride, which allow reversible and energy-efficient tuning[72]. The selection of material depends on factors such as desired modulation speed, power efficiency, scalability, and the specific requirements of applications like optical switching, sensing, and reconfigurable photonic circuits.

Table 1. Key characteristics of TO materials.

Material	Key Characteristics	Advantages	Challenges
Si [45]	High TOC, widely used in integrated photonics, CMOS-compatible	Well-established fabrication process, cost-effective, easy integration with existing semiconductor tech	Low TOC compared to other materials, sensitivity to temperature fluctuations, and limited wavelength range
SiN [73]	High thermal stability, low loss in the visible to near-infrared range, relatively high TOC	Low-loss, high-performance for visible and near-infrared, compatible with standard photonic integration	Higher fabrication complexity, less widely used in industry compared to Si
LN [65]	High EO and TOCs, high-index contrast	Strong TO effect, suitable for high-performance photonic devices, widely used for modulators	Expensive, difficult to integrate with Si, handling issues due to fragility
Silicon Carbide (SiC)[74]	High thermal conductivity, wide bandgap, stable at high temperatures	Extremely high thermal stability, works well in harsh environments, good for high-power applications	Expensive, difficult to process and integrate with other materials, and not widely used in photonics
Polymer-based materials (e.g., PMMA, SU-8)[46]	Moderate TOCs, flexible, lower refractive index contrast	Cost-effective, flexible, easy to process, adaptable for low-loss devices, and integration with flexible substrates	Lower TOCs compared to inorganic materials, lower stability under temperature cycling
Gallium Arsenide (GaAs)[75]	High TOC, widely used in optoelectronics	High performance in photonic devices, used for high-speed communications and optical switching	Difficult to integrate with Si, expensive, challenging to scale for large-scale photonic circuits
Chalcogenide Glasses[47,76]	High refractive index, large TOCs, used in infrared photonics	Excellent performance in the infrared range, suitable for	Not CMOS-compatible, expensive, and difficult

 doi:10.20944/preprints202505.0911.v1

	nonlinear optics and low-loss waveguides	to manufacture on a large scale

A compact light modulator based on Si photonic crystal (PhC) technology was designed, fabricated, and experimentally validated for operation near the 1.55 μm wavelength under TE polarization[64]. The core mechanism relied on tuning the cutoff frequency of a line-defect PhC structure, which was sensitive to changes in the Si refractive index. This tuning was achieved through localized thermal modulation, exploiting Si's strong TO effect. The PhC consisted of a triangular lattice of cylindrical air holes etched into a SOI platform. Optical measurements confirmed effective TO control of the cutoff frequency, demonstrating the device's potential for wavelength-selective modulation[64].

Maeder et al. explored the impact of geometry on the performance of metal strip TO phase shifters (TOPSs), both through modeling and experimental characterization[77]. To validate the simulated geometries, imbalanced Mach-Zehnder interferometers (MZIs) were fabricated on a 600-nm X-cut LNOI chip. The chip featured a 2-μm SiO_2 insulation layer and a 500-μm Si handle. Ridge waveguides with a 1-μm width were formed by etching 200 nm of the LN layer, as illustrated in Figure 3 (a, b)[77]. The results showed a 10-fold reduction in the voltage-length product compared to EO phase shifters (EOPSs), with bandwidths exceeding 100 kHz. Additionally, the footprint remained minimal, demonstrating the potential of TOPSs as efficient, small-scale building blocks for stable tuning and switching in LNOI photonic circuits.

Valley photonic crystals (VPCs) have been investigated as an effective means to suppress backscattering and support robust light propagation through sharp bends, offering a viable route to realizing compact and low-loss components for integrated optical communication systems. However, limited research has been conducted on enabling power-efficient tunable functionalities in VPC-based devices, which are crucial for implementing essential operations such as optical switching and routing. Sun et al. proposed a thermally tunable add-drop filter (ADF) based on VPCs and experimentally verified at telecommunication wavelengths[78]. Topologically protected edge states and the negligible scattering associated with sharp bends were exploited to achieve a minimized device footprint of 17.4 × 28.2 μm^2 and a low insertion loss of 2.7 dB. A diamond-shaped micro-loop resonator was introduced to confine optical modes and enhance thermal interaction through a microheater. As a result, a switching power of only 23.97 mW was required to redirect the output signal between ports. High-speed data transmission at a rate of 132 Gb/s was demonstrated using the thermally tuned ADF, with performance preserved under topological protection. These results have shown that thermally tunable VPCs based on Si can be utilized to develop reconfigurable, topologically protected photonic devices suitable for next-generation on-chip communication systems[78].

A thermo-optically tunable optical filter was designed and fabricated on a lithium niobate on insulator (LNOI) platform, which offers strong optical confinement while preserving the advantageous properties of LN[65]. The filter was implemented using two cascaded racetrack MRRs, a configuration selected to achieve high spectral performance (Figure 3 (c)). As shown in Figure 3 (d), the ridge waveguide has a 260 nm etching depth, 1.2 μm width, and 72° sidewall angle for single-mode operation. A 1 μm top cladding isolates the MRRs from the heaters, minimizing optical loss. The micro-heater has a Ti thickness of 150 nm and a width of 2.5 μm.

A flat-top passband with an intra-band ripple of less than 0.3 dB was obtained, along with a 3 dB bandwidth of 4.8 GHz and an out-of-band rejection of approximately 35 dB. The total insertion loss was measured at around −14 dB, comprising roughly −6.5 dB from grating coupler losses and less than −1 dB from on-chip losses. A center wavelength shifts over one free spectral range (FSR) was achieved using a heating power of approximately 89.4 mW. This device has been identified as a suitable candidate for use in optical signal processing and microwave photonic applications due to its tunability and high filtering performance[65].

 doi:10.20944/preprints202505.0911.v1

Ultra-broadband, low-loss TO switches were recently demonstrated on a Si platform, employing a 2 × 2 MZI structure integrated with bent directional couplers[79]. These MZI-based switches were further scaled to N × N configurations and were integrated with arrayed waveguide gratings to realize compact reconfigurable add-drop multiplexers. To improve thermal tuning efficiency, a transparent graphene nano-heater directly contacting the Si core was experimentally implemented and validated. These advancements have established new possibilities for developing high-performance, thermally tunable PICs on Si[79].

An on-chip TO switch was efficiently designed and validated through experiments, incorporating a photonic crystal nanobeam cavity (PCNC) in conjunction with a microheater made of hydrogen-doped indium oxide (IHO) [80]. The compact mode volume of the PCNC, along with the localized heating effect enabled by the transparent and conductive IHO, significantly boosts the interaction between thermal and optical fields, thereby enhancing TO tuning performance. A top-view schematic of the device, shown in Figure 3(e), features a waveguide patterned with 40 air holes arranged symmetrically. These holes define a central graded region flanked by two reflector sections. Each reflector, comprising 13 air holes, generates a photonic bandgap that confines light within the central cavity. This central region is engineered to minimize scattering and ensure efficient phase matching. For high extinction ratio (ER) operation, the widths of the nanobeam and its adjacent waveguide are set to 500 nm and 380 nm, respectively, with 225 nm spacing. Figure 3(f) illustrates the simulated resonant electric field distribution, highlighting that the optical field is concentrated in the 14-hole central zone, yielding an effective TO tuning length of approximately 4 μm [80].

Figure 3 (g) presents an SEM image of the coupled waveguide and central gradient region. Figure 3 (h) compares cross-sectional views of TO switches with conventional metal and IHO microheaters. The conventional switch uses a 100 nm NiCr alloy microheater with a 1 μm thick SiO_2 layer, while the IHO microheater, made from a 70 nm thick IHO film, reduces absorption loss. The SiO_2 isolation layer is thinner (200 nm) to improve heat conduction without affecting optical resonance in the PCNC. Experimental results reveal a TO tuning efficiency of 1.326 nm/mW, with measured rise and fall times of 3.90 μs and 2.65 μs, respectively. The extinction ratios of the switches, measured at 25.8 dB and 27.6 dB, show that the IHO microheater introduces negligible insertion loss compared to conventional metal microheaters. This work demonstrates the strong potential of the TO switch as a critical unit for large-scale on-chip integrated arrays[80].

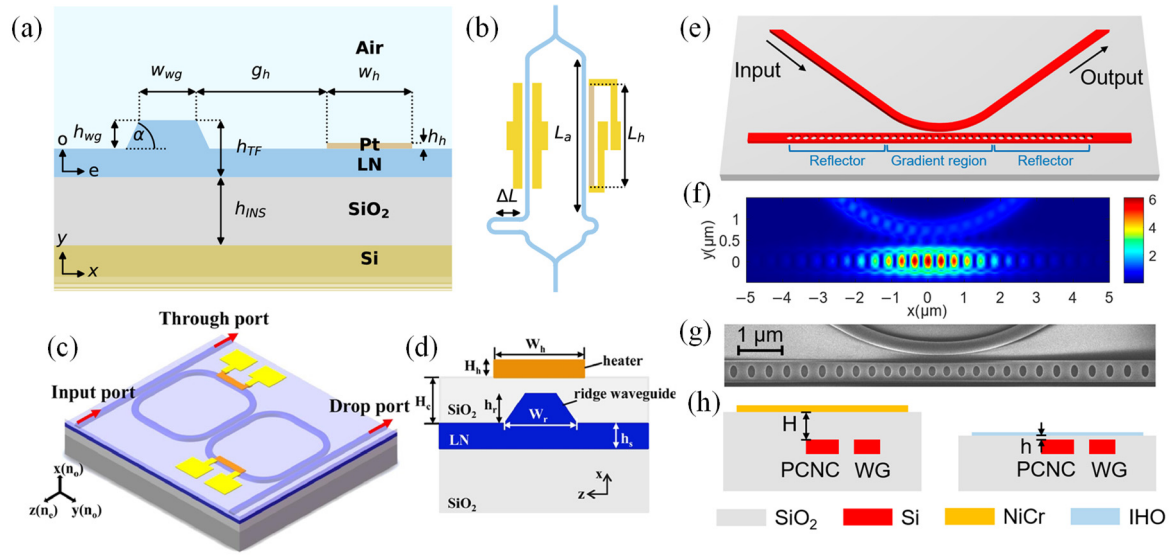

Figure 3. (a) Cross-sectional diagram of the TOPS, featuring the LNOI ridge waveguide and the platinum (Pt) heater layer[77], (b) Asymmetric MZI configuration, where the first arm incorporates an EOPS and the second arm uses a TOPS, enabling a comparison between the two phase-shifter types[77], (c) Schematic representation of the LNOI TO tunable optical filter[65], (d) Cross-sectional view illustrating the waveguide and heater structure[65], (e) Diagram illustrating the structure of the PCNC[80], (f) Simulation of the electric field

 doi:10.20944/preprints202505.0911.v1

distribution within the PCNC at the resonant wavelength[80], (g) SEM image showing the PCNC[80], (h) Simplified cross-sectional view of the TO switch, with waveguide (WG) labeled[80].

4. Key Material Classes for EO Applications

Key EO materials for tunable photonic devices are chosen based on their ability to efficiently change refractive index in response to an electric field, enabling high-speed and low-power modulation (Table 2) [31,81]. LN is a leading material due to its strong linear EO effect, broad optical transparency, and stable performance, making it ideal for modulators and switches[22,54]. Gallium arsenide[82] and indium phosphide[83] are also widely used, especially in high-frequency applications, because of their high electro-optic coefficients (EOCs) and compatibility with active photonic components like lasers and detectors. EO polymers offer advantages such as low voltage operation, fast response, and ease of processing, making them suitable for flexible and compact devices[84]. BTO provides very high EO activity and is being explored for integrated platforms, although it presents fabrication challenges[56]. Recent advances in thin-film LN have further improved integration, allowing for compact, efficient, and scalable devices[54]. The selection of material depends on the specific requirements of the application, including speed, footprint, integration method, and operating wavelength.

As global data traffic continues to grow, the demand for high-bandwidth, energy-efficient communication systems intensifies. While current optical networks effectively handle data transmission over long and medium distances, the need for low-cost, scalable short-reach interconnects has brought Si photonics to the forefront. Its potential for mass production and integration makes it a strong candidate for next-generation chip-scale optical systems. A key challenge in this space is achieving efficient electrical-to-optical signal conversion using modulators that are both compact and high-speed. In response, Brimont et al. presented a Si-based EO modulator that combined slow-light enhancement in a nanostructured periodic waveguide with a high-speed semiconductor pn junction. Slow light was implemented using a 1D periodic waveguide with alternating narrow (W = 300 nm) and wide (We = 650 nm) segments, repeated every 310 nm (Figure 4 (a, b)). The waveguide height was 220 nm, leaving a 100 nm-thick slab after partial etching (Figure 4 (c, d)). Phase modulation was achieved via a reverse-biased pn junction formed near the waveguide core. Heavily doped p+ and n+ regions placed 500 nm (S_p) and 550 nm (S_n) from the waveguide edge, were contacted using AlCu electrodes. Doping concentrations are 3×10^{17} cm^{-3} (p), 1.5×10^{18} cm^{-3} (n), and 1×10^{20} cm^{-3} (p+, n+). This synergistic design enabled a highly efficient, 500 μm-long modulator capable of error-free data transmission at 20 Gbit/s. Moreover, the device demonstrated the potential for modulation rates up to 40 Gbit/s, underscoring its suitability for future low-power, high-density photonic interconnects. These results established a promising pathway toward ultrafast, scalable networks-on-chip, enabling the next generation of high-performance computing systems[85].

 doi:10.20944/preprints202505.0911.v1

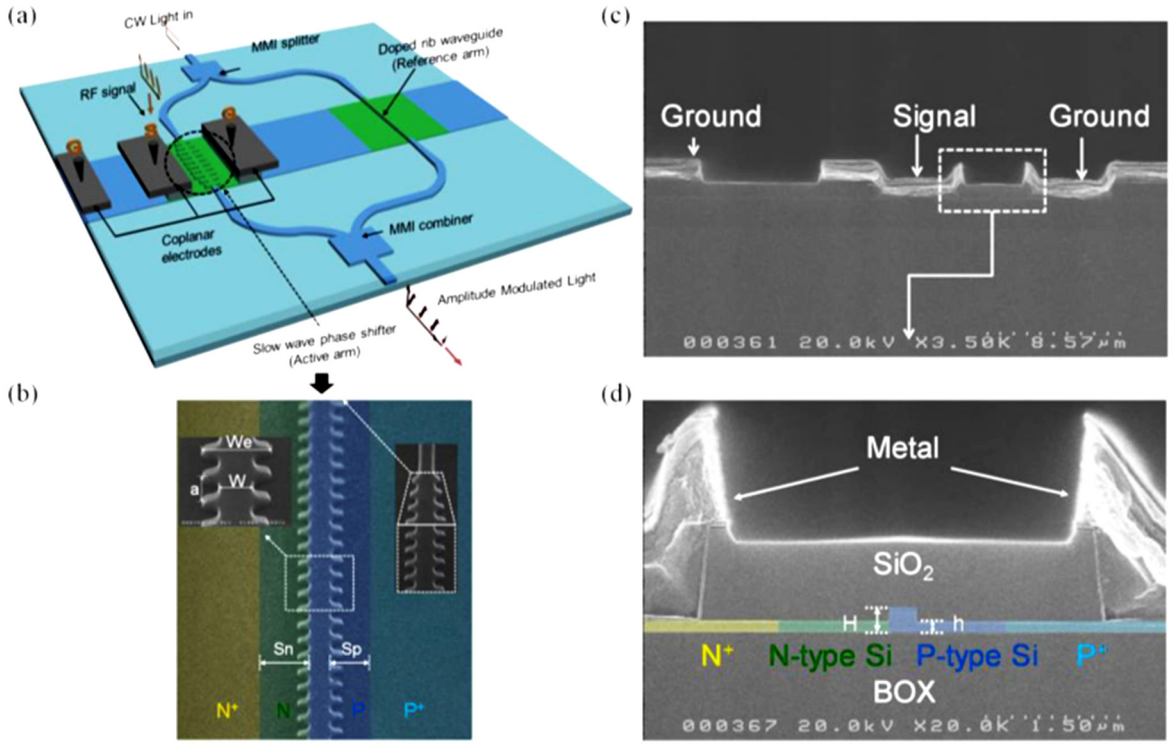

Figure 4. (a) Schematic of the modulator using an asymmetric MZI with MMI couplers for light splitting and combining, (b) Transverse SEM image showing the device layout and ground-signal-ground (GSG) coplanar electrodes, (c, d) Top and cross-sectional SEM views of the corrugated waveguide. The left inset highlights the taper for low-loss coupling between rib and slow-light sections; the right inset zooms into the corrugated structure. Doped regions are marked in color[85].

Zhang et al. presented a novel strategy for achieving significant miniaturization of these modulators by leveraging topological photonics[86]. This design utilized a one-dimensional topological interface state implemented on a thin-film LN integrated platform. This configuration enabled strong optical confinement and a pronounced EO enhancement at the topological interface. As a result, a topological cavity with a compact footprint of just 1.6 × 140 μm² was realized, achieving an exceptional modulation bandwidth of 104 GHz. This represents the most compact LN-based modulator with a bandwidth exceeding 28 GHz. The device supported high-speed signal generation, including 100 Gb/s non-return-to-zero (NRZ) and 100 Gb/s four-level pulse amplitude modulation (PAM4). Owing to the reduced mode volume and low device capacitance, the modulator achieved an ultralow switching energy of 5.4 fJ/bit. By reducing the response time of topological photonic devices from the microsecond to the picosecond regime, this work established a foundation for scalable, high-speed LN PICs[86].

Table 2. Key characteristics of EO materials.

Material	Key Characteristics	Advantages	Challenges
LN [87,88]	Benchmark EO material; Advances in thin-film and LNOI platforms	High EO efficiency; Wide transparency window (0.4–5.5 μm); Mature fabrication techniques	CMOS integration is challenging due to material incompatibility[22]
EO Polymers[89]	High-speed modulation potential; Organic	Ultrafast response; Potential for flexible integration	Stability issues under high temperatures; Integration

 doi:10.20944/preprints202505.0911.v1

	materials with tunable properties		challenges with CMOS processes[84]
BTO & Perovskites[90]	High EOCs (e.g., $r_{42} \approx$ 923 pm/V); Emerging perovskite materials	Strong modulation performance; Compatibility with CMOS platforms [91]	Material stability and uniform deposition remain a challenge
III–V Semiconductors (GaAs, InP)[92]	Active modulation with integrated electronics; Wavelength-dependent performance	Direct bandgap materials enable efficient light emission; Integration of active components like lasers and detectors	Limited CMOS compatibility; Performance varies with wavelength [89]

5. Device Architecture and Integration Platforms

The ability to manipulate light in photonic devices using EO and TO effects is pivotal in many modern applications, including telecommunications, sensing, and information processing[68,93]. The integration of various materials and the choice of platform for these devices significantly impact their performance, scalability, and potential applications. In this section, key considerations and innovations in device architectures and integration platforms are discussed, focusing on waveguides[37], modulators[22], switches[18], and tunable filters[94], as well as bulk vs. thin-film integration, heterogeneous integration, and the role of plasmonics[61] and metasurfaces (MS)[95].

5.1. Waveguides, Modulators, Switches, and Tunable Filters

Waveguides are essential components in integrated photonics, guiding light through a structured medium[96,97]. Modulators exploit the EO effect to change the phase, amplitude, or frequency of the optical signal by applying an external electric field. These devices, often based on MZI [86,98,99], electro-absorption modulators (EAM)[100–102], or micro-MRRs [103,104], enable high-speed optical communication systems. Switches, on the other hand, utilize the modulation of light to enable the routing of optical signals, and tunable filters offer wavelength-selective filtering, which is particularly useful for wavelength division multiplexing (WDM) in optical networks[33,105,106]. The integration of EO and TO tuning mechanisms into these devices significantly improves their versatility and response times.

Li et al. presented a compact, electro-optically tunable optical filter designed on an LNOI platform, utilizing sidewall long-period waveguide gratings (LPWGs)[94]. Figures 5 (a) and 5 (b) present the schematic representations of the device in three-dimensional and top views, respectively. The filter architecture incorporated two key components: corrugated sidewall LPWGs to enable mode coupling, and metal ribbons for absorption, with a tapered waveguide facilitating the filtering process. This combination allowed precise control over light propagation within the waveguide. Each grating structure on the sidewalls is defined by a common set of parameters. These include the grating period (Λ), the etch depth (d), a relative phase shift of one-half period between the two gratings, and a duty cycle of 50 percent. EO tuning is achieved using a pair of chromium and gold electrodes that were aligned along the length of the two-mode rib waveguide. These electrodes were separated from the waveguide by a silicon dioxide buffer layer with a thickness (h_c), as shown in Figure 5 (c). The spacing between the electrodes is labeled as (w_e), and their length is equal to that of the two-mode waveguide section.

Figure 5 (d) shows the normalized transmission spectra measured at 25 degrees Celsius. As the voltage increases from 0 to 20 volts, the center wavelength redshifts from 1587.1 to 1593.7 nm, with the contrast decreasing from 16.32 to 13.68 decibels. When the voltage decreases to minus 13 volts,

 doi:10.20944/preprints202505.0911.v1

the center wavelength blueshifts to 1582.8 nm, with the contrast dropping to 11.66 decibels before rising to 15.22 decibels. Figure 5 (e) confirms a near-linear shift in center wavelength with a tuning rate of approximately 0.344 nm per volt, while the contrast variation remains nonlinear, as seen in Figure 5 (d). The thermal response of the packaged filter was examined by observing how the center wavelength of the rejection band changes with ambient temperature. Normalized transmission spectra were recorded at various temperatures ranging from 25 to 55 degrees Celsius, as shown in Figure 5 (f). As the temperature increased within this range, the center wavelength shifted to shorter values, moving from 1587.1 nm to 1582.9 nm. This blueshift followed an approximately linear trend, with a rate of about 0.137 nm/°C, as depicted in Figure 5 (g). Due to its compact form and compatibility with other LNOI-based components, this filter is well-suited for integration into more complex photonic circuits aimed at advanced on-chip optical signal processing[94].

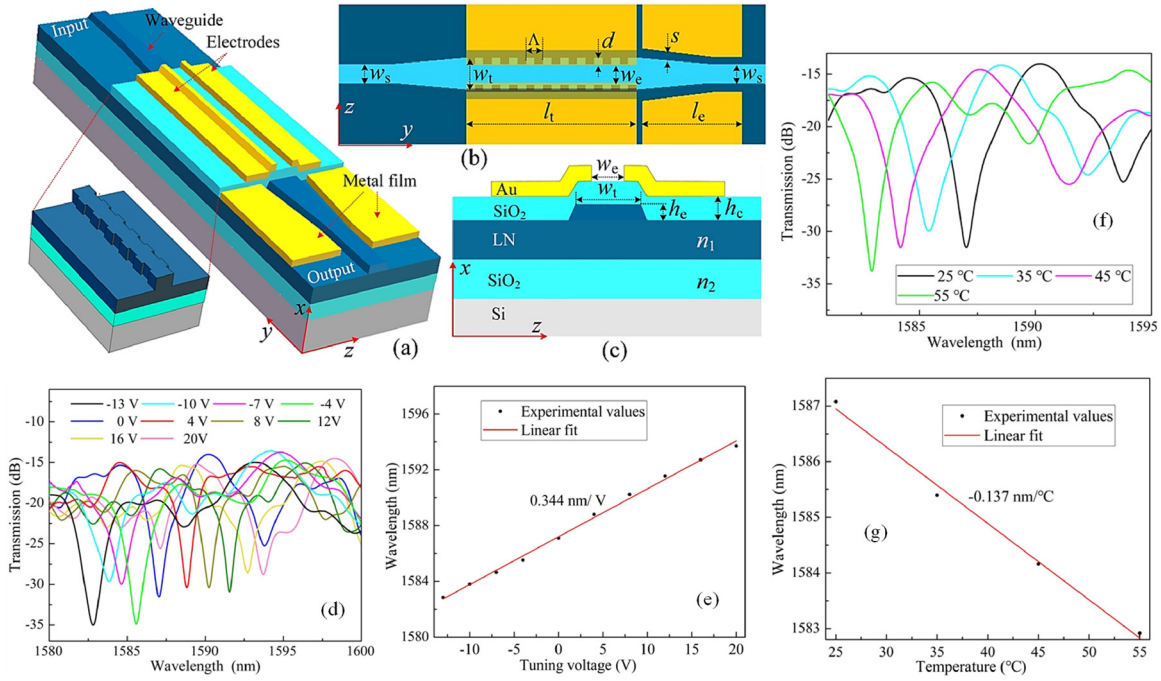

Figure 5. (a) Diagram of the LPWG filter, (b) top view layout, and (c) cross-section of the EO tuning area. The inset in (a) shows asymmetric gratings on the ridge sidewalls without the buffer layer and electrodes, (d) Transmission spectra at tuning voltages from −13 to 20 volts, (e) center wavelength shift with voltage and linear fit, (f) Transmission spectra at temperatures from 25 to 55 degrees Celsius, (g) center wavelength shift with temperature and linear fit[94].

5.2. Bulk vs. Thin-Film Integration

The integration of photonic devices can be approached through two primary strategies: bulk integration and thin-film integration. In the bulk integration approach, waveguides and other photonic components are fabricated on large substrates with relatively thick layers of material, such as LN or bulk crystals[32]. Bulk materials typically offer high nonlinearities and strong EO effects, making them suitable for high-performance modulators and switches[107]. However, the scalability of bulk devices in integrated photonics is limited by their size, weight, and fabrication complexity[81].

Thin-film integration, which involves the deposition of thin layers of materials onto substrates like Si, SiN, or glass, has become more dominant in recent years[108–110]. Thin-film devices allow for greater miniaturization, reduced material usage, and easier integration with existing semiconductor fabrication technologies[111]. Materials like Si, SiN, and polymers are widely used for this purpose, as they provide a range of optical properties and enable compact, scalable photonic circuits[112]. Thin-film integration is particularly attractive for large-scale PICs, which can be fabricated using standard photolithographic techniques[113]. The trade-offs between these integration platforms often come down to factors like device performance, ease of integration, and

 doi:10.20944/preprints202505.0911.v1

cost. While bulk materials provide superior optical properties, thin-film devices offer flexibility and scalability suitable for high-density integration[112].

Thin-film lithium niobate (TFLN) EO modulators have emerged as leading candidates for advancing modern photonic systems. By leveraging the inherent strengths of LN, such as minimal optical loss, high signal extinction, excellent linearity, and strong optical power tolerance, these devices outperform traditional bulk modulators in key areas. In particular, TFLN modulators significantly enhance voltage-to-bandwidth efficiency. Despite these advantages, their compact electrode spacing introduces considerable microwave attenuation due to metal-induced absorption, which restricts performance at higher frequencies[114].

To address this, Tao et al. engineered traveling-wave electrodes with precision microstructures, successfully extending the 3 dB EO bandwidth to 51.2 GHz[114]. Figure 6 presents the schematic of the nanophotonic LN modulator in panel (a), with the cross-sectional (b) and top (c) views of the electrode design shown in the following panels. The fabricated devices also demonstrated excellent performance metrics, including sub-2 dB optical insertion loss and a 15 dB extinction ratio. Encapsulated in metal packages, the modulators underwent and passed comprehensive reliability assessments. This development marked a pivotal milestone in bringing TFLN modulator technology closer to widespread application and commercial viability[114].

The modulator (Figure 6 (d, e)) was housed in a 45×20×9 mm Kovar package, selected for thermal compatibility and sealed with nickel and gold plating. Inside, space was machined for the LN chip and microwave components. Optical feedthroughs use Kovar tubes. To reduce coupling loss from mode mismatch, polarization-maintaining fibers with smaller cores and on-chip spot-size converters were used. Precision alignment within 0.1 μm and 0.05° was achieved using a six-axis platform. UV adhesive and solder secure the fibers, maintaining over 20 dB polarization extinction. The actual coupling loss was around 20 dB. RF signals enter via 1.85 mm connectors rated to 65 GHz. A coplanar waveguide on an aluminum nitride substrate routes signals to the modulator, which was gold-wire bonded. Good grounding and 50 Ω termination resistors ensure low return loss. Seam welding seals the package, with helium leak testing confirming integrity[114].

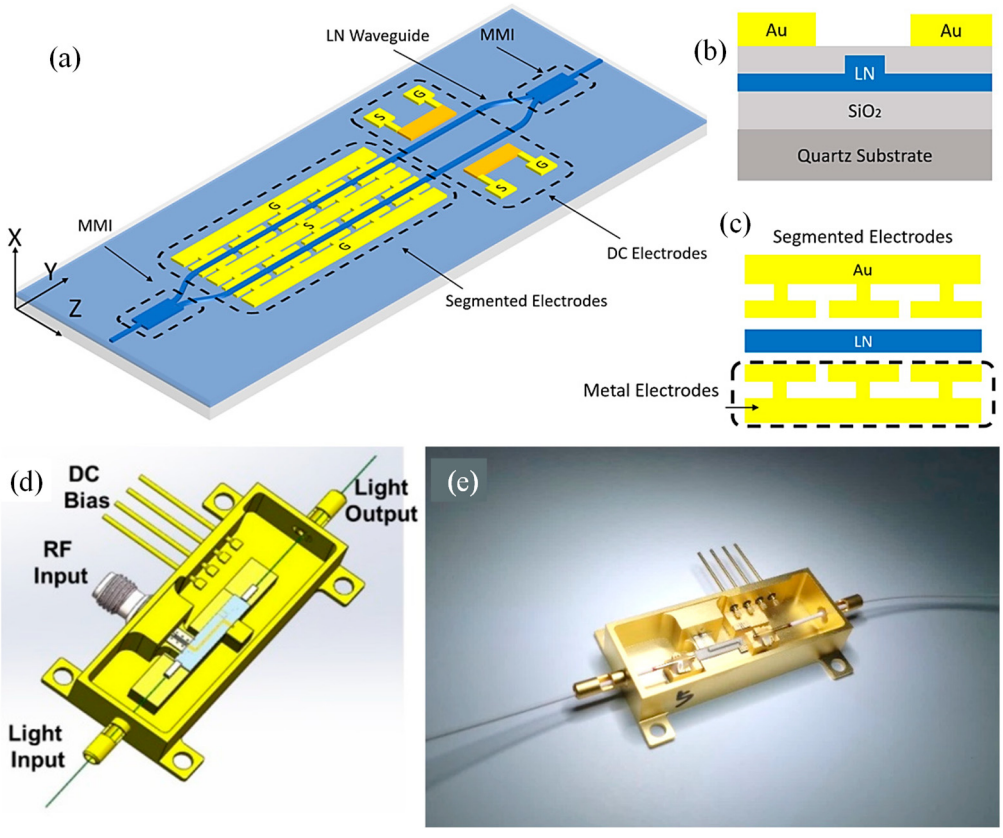

 doi:10.20944/preprints202505.0911.v1

Figure 6. (a) Illustration of the LN modulator architecture, (b) detailed cross-sectional representation of the electrode segmentation, (c) overhead view highlighting the electrode arrangement. Internal configuration of the EO modulator package: (d) conceptual layout and (e) corresponding physical images[114].

5.3. Heterogeneous Integration and Hybrid Material Systems

Heterogeneous integration refers to the combination of different materials or technologies to create a composite device with complementary properties[115,116]. In the context of tunable photonics, heterogeneous integration enables the use of a range of materials, such as Si for efficient waveguiding and EO materials like LN or III-V semiconductors for fast modulation[117,118]. This allows for devices that leverage the strengths of each material while mitigating individual limitations[119,120].

For example, hybrid integration of Si photonics with LN offers an attractive path for developing high-performance modulators and switches that can operate at high speeds, while still maintaining the compactness and scalability of Si[121,122]. This integration can also facilitate the combination of passive waveguides with active modulation regions, allowing for high-density photonic circuits with reduced power consumption. III-V semiconductor materials, such as indium phosphide (InP) and gallium arsenide (GaAs), can be integrated with Si to provide active devices like lasers and modulators, further enhancing the capabilities of photonic circuits[123–126].

Moreover, hybrid material systems can incorporate novel 2D materials such as graphene or transition metal dichalcogenides (TMDs), offering unique optoelectronic properties that are leveraged in tunable photonic devices[127–129]. These materials enable lower-power modulation, greater integration flexibility, and new functionalities, including tunable absorption, phase shifting, and enhanced light-matter interactions.

Advances in precision measurement technologies such as atomic clocks, inertial navigation systems, and experiments probing the foundations of physics have led to increasingly stringent demands on laser frequency noise. Rubidium-based quantum systems require highly stable 780-nanometer lasers for optimal performance in timing, sensing, and quantum information processing. While these systems currently rely on discrete, tabletop laser setups, achieving wafer-level integration is essential for enabling compact and scalable photonic systems suitable for integration into chip-scale platforms.

Despite ongoing efforts to develop integrated 780-nanometer lasers with extremely narrow linewidths, achieving both a fundamental linewidth below one hertz and an integral linewidth under one kilohertz has remained a difficult goal. Isichenko et al. presented a hybrid integrated laser operating at 780 nm that demonstrates significant progress toward overcoming this challenge[130]. The laser utilized a self-injection locking technique and achieved a fundamental linewidth of 0.74 hertz and an integral linewidth of 864 hertz. Additionally, the laser reaches a thermorefractive noise floor of 100 hertz squared per hertz at a 10-kilohertz offset, representing over an order of magnitude improvement compared to prior integrated devices operating at the same wavelength.

The chip-scale self-injection locked (SIL) laser system integrated a commercial 780 nm Fabry-Pérot laser diode (FPLD) with an ultra-high-Q SiN photonic chip. The FPLD, supplied in a TO-can package, was modified by removing its lid and is edge-coupled to the chip (Figure 7 (a, b)). To align with the transverse magnetic (TM) waveguide mode selected for its lower propagation loss, the diode was rotated by 90 degrees during coupling. The integrated chip comprised a high-Q MRR, a power splitter, and a thermal phase tuner. All components were fabricated using a CMOS-compatible SiN process. Near-critical coupling between the resonator and waveguide achieved a 20 dB extinction ratio. Combined with an intrinsic quality factor of 90 million, this facilitates strong resonant Rayleigh backscattering, which provides narrowband optical feedback to the laser. Using an unbalanced MZI, the resonator was measured to have an intrinsic Q of 90 million and a loaded Q of 43 million. These values correspond to a 0.57 dB/m propagation loss and a linewidth of 8.9 MHz (Figure 7 (c)). The resonator had a 5 mm radius, yielding a free spectral range (FSR) of 6.43 GHz.

 doi:10.20944/preprints202505.0911.v1

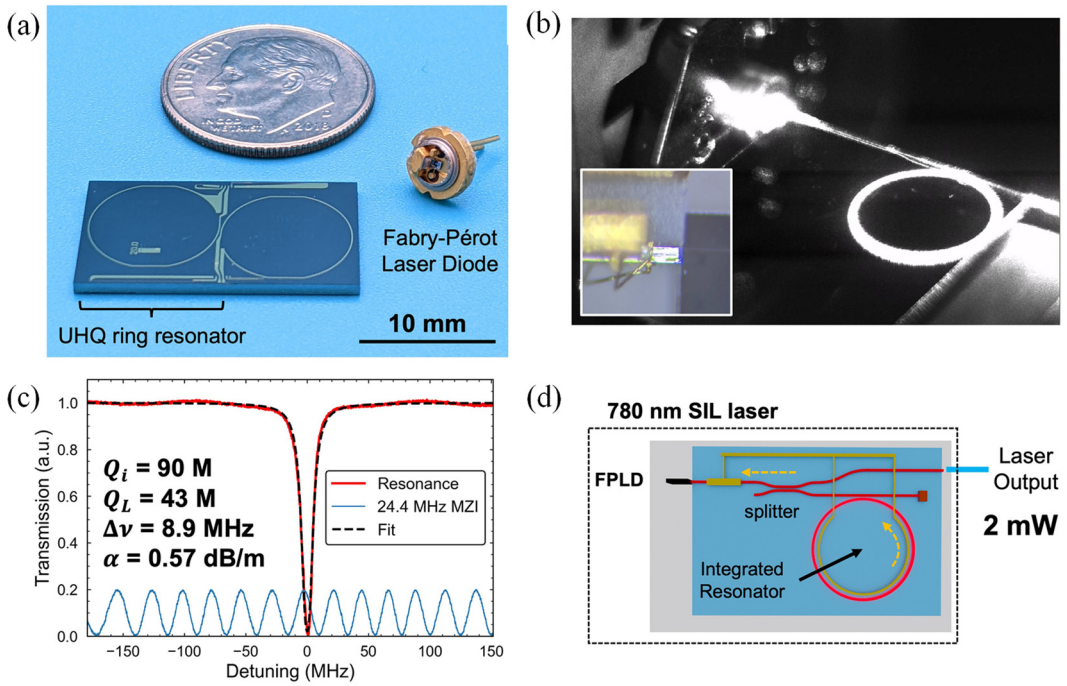

Figure 7. Hybrid-Integrated 780 nm Self-Injection Locked Laser: (a) Image of the chip-scale laser system, featuring an ultra-high-Q MRR and a Fabry-Pérot laser diode (FPLD), shown with a dime for scale, (b) Laser output locked to the resonator. Inset shows angled edge coupling of the FPLD, (c) Resonator transmission spectrum showing a loaded Q of 43 million, intrinsic Q of 90 million, 0.57 dB/m loss, and 8.9 MHz linewidth. Frequency calibration is done using an unbalanced MZI (blue trace), (d) Schematic of the self-injection locked laser: the FPLD is edge-coupled to a chip with a splitter and a thermally tunable high-Q resonator. Output is collected through an edge-coupled cleaved fiber[130].

The system supported two configurations: one optimized using a multi-axis alignment stage, and another in which the laser was permanently bonded to the chip in a hybrid package. Optical feedback from the resonator was strong enough to allow efficient power extraction via an on-chip directional coupler, delivering 2 mW output power (Figure 7 (d)). This output was over ten times higher than earlier chip-scale SIL lasers with comparable frequency noise performance. To enhance coupling, the waveguide width was tapered from 4 μm near the resonator to 2 μm at the chip edge. The measured coupling loss between the FPLD and the chip was approximately 4 dB. The demonstrated performance illustrates the potential of this laser architecture for enabling compact and low-noise light sources suitable for a wide range of quantum sensing, computation, and metrology applications. Furthermore, the design principles can be extended to other atomic transition wavelengths, opening new opportunities for integrated quantum systems[130].

5.4. Role of Plasmonics and MS in Enhancing Effects

Plasmonics and MS have emerged as powerful tools in the field of photonics, providing new avenues for enhancing the EO and TO effects[95]. Plasmonics exploits the interaction between electromagnetic waves and free electrons in metal nanostructures to concentrate light into subwavelength volumes[131]. This can lead to enhanced light-matter interactions, particularly in miniaturized devices such as modulators and sensors[132–134]. In tunable photonic devices, plasmonic structures can be used to achieve stronger EO and TO effects by amplifying the local electric field or heat generation in the vicinity of the metal structures[135]. This allows for more efficient modulation and switching, with the potential for ultra-fast response times. Plasmonic modulators, for instance, exploit the strong field confinement of surface plasmon polaritons to enable high-speed, low-power modulation of light[61,135].

 doi:10.20944/preprints202505.0911.v1

MS, which are engineered 2D materials with subwavelength patterns, offer another promising approach for enhancing tunable photonic devices. MS can control the phase, polarization, and intensity of light on demand, making them ideal for applications in beam shaping, tunable filters, and dynamic holography[8,136–138]. By carefully designing MS with EO or TO materials, it is possible to achieve high-performance, low-loss tunable devices that offer both structural and material flexibility. In some designs, the combination of EO materials with MS has led to devices that can dynamically control light propagation through induced changes in both phase and amplitude, creating tunable filters and modulators with low energy consumption[139,140].

Zhang et al. experimentally demonstrated a high-speed EO modulator based on a plasmonic MS, designed to function in the near-infrared spectral region with gigahertz-level modulation bandwidth (Figure 8 (a))[141]. To enable effective intensity modulation of reflected light, a carefully engineered subwavelength grating composed of alternating metal and insulator layers was employed. This structure supported bimodal plasmonic resonances, which were tuned to meet the condition for critical coupling. As a result, the device achieved near-total light absorption, measured at 99.8 % or −27 dB, and exhibited a high-quality resonance with a Q factor of 113 at a wavelength of 1650 nm[141].

Figures 8 (b) and 8 (c) display the top-view optical image and the SEM image of the fabricated device featuring a grating period of 1080 nm. For testing and measurement purposes, the device was wire-bonded onto a printed circuit board (PCB). The integration of an EO polymer within the grating enables a modulation depth of up to 9.5 decibels when a voltage of ±30 volts was applied. The modulator demonstrated a 3-decibel bandwidth of 1.25 gigahertz, with performance primarily limited by contact resistance and the output impedance of the driving circuit. Due to the high electrical conductivity of the metallic components and the compact structure that minimizes parasitic capacitance, the device holds strong potential for operation at frequencies well above the current bandwidth. This advancement opens new possibilities for ultrafast active MS in a wide range of optical and photonic applications[141].

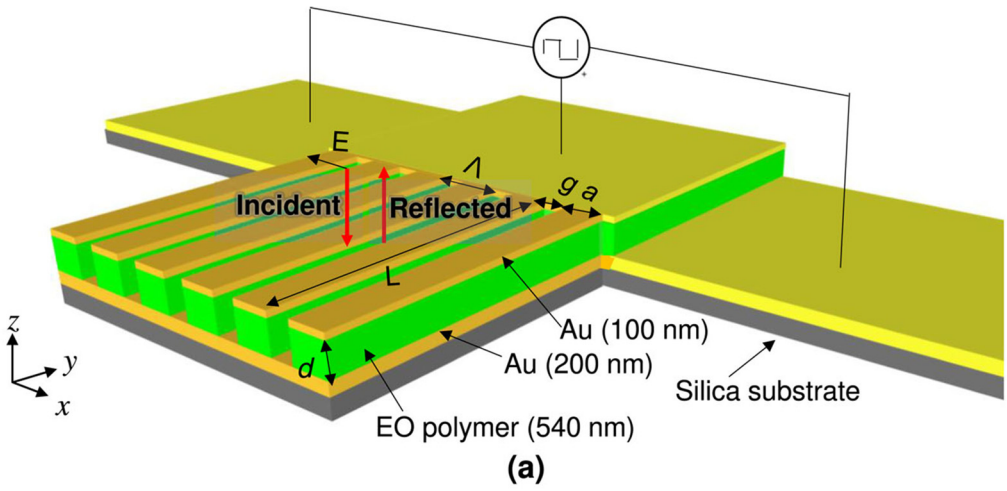

(a)

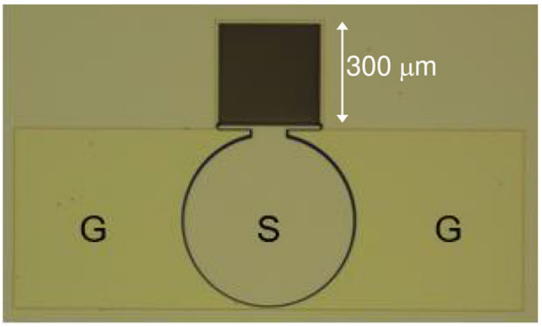

(b)

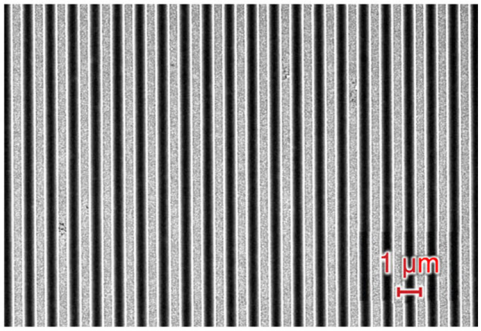

(c)

 doi:10.20944/preprints202505.0911.v1

Figure 8. Overview of the MS Modulator Configuration: (a) A schematic illustration presents the overall structure of the device, (b) An optical microscope image captures the top view of the fabricated MS, (c) A top-down SEM image reveals the detailed features of the grating, which has a periodicity of 1080 nm[141].

6. Performance Metrics and Comparison

The performance of tunable photonic devices based on EO and TO materials is assessed using a range of key metrics that determine their efficiency, practicality, and long-term viability in real-world applications. These metrics include tuning efficiency, insertion loss, modulation bandwidth and speed, power consumption, and long-term stability.

6.1. Tuning Efficiency

Tuning efficiency quantifies how effectively a device can alter its resonant or operational wavelength in response to external stimuli such as temperature or voltage[14,142,143]. It is typically expressed as the change in wavelength per unit temperature ($d\lambda/dT$) for TO materials or per unit voltage ($d\lambda/dV$) for EO materials. TO materials often exhibit higher tuning efficiency due to the relatively large TOC of certain polymers and semiconductors[5,144]. For example, Si has a TOC of approximately 1.86×10^{-4} per Kelvin, resulting in a substantial shift in resonance with moderate temperature changes. Besides, Chen et al. proposed a thermally tunable nanobeam cavity made of SiN, embedded within a polymer[144]. This device exhibits a tuning efficiency of 44 pm/°C and 0.13 nm/mW in the near-visible spectrum. The impressive tuning performance is driven by two factors: the high TOC of the SU-8 polymer and the unique "air-mode" cavity design, which allows a significant portion of the cavity's optical field to be confined within the polymer region. This resonator offers a promising platform for localized tuning in cavity quantum electrodynamics experiments based on SiN[144]. Furthermore, EO materials such as LN demonstrate faster but often smaller shifts in wavelength per unit voltage due to the lower index modulation achievable via the Pockels effect[22]. The choice between these two mechanisms depends on the specific requirements for speed versus tuning range.

Li et al. presented high-speed LN EO modulators built using photonic crystal nanobeam resonators (Figure 9 (a))[22]. These devices offered strong performance characteristics, including a high tuning efficiency of 1.98 GHz/V, a wide 17.5 GHz modulation bandwidth, and a minimal EO mode volume of just 0.58 μm^3. The modulators efficiently drive high-Q cavity modes across both adiabatic and non-adiabatic regimes. Figure 9 (b) shows the modulation response of one of the devices (blue curve), revealing a 3-dB bandwidth of approximately 17.5 GHz. This bandwidth is primarily constrained by the photon lifetime of the EOM cavity (~11 ps), as the electrode circuit's broader spectral response is evident from the flat S_{11} reflection spectrum shown in Figure 9 (b).

Since the modulation bandwidth was mainly determined by the device's optical Q, it can be easily adjusted for various applications by selecting devices with the desired optical Q. For comparison, the orange curve in Figure 9 (b) illustrates a device with an optical Q of 20,000, which achieves a 3-dB bandwidth of around 12.5 GHz. The wide modulation bandwidth of these devices enables high-speed EO switching. To demonstrate this, an NRZ signal was applied with a (2^7-1)-bit pseudo-random binary sequence (PRBS) to an EOM with a V_{pp} of 2.0 V. The resulting eye diagrams at two-bit rates, 9 and 11 Gb/s, are shown in Figures 9 (c) and 9 (d), respectively. Both diagrams exhibit clear eye openings, indicating successful high-speed operation. The demonstrated bit rates were limited by the maximum bit rate of the PRBS generator (Agilent 70843B), which caps at 12 Gb/s. However, the minimal degradation observed between Figures 9 (c) and 9 (d) suggests that the EOM could support even higher bit rates. This work lays the groundwork for large-scale LN-based photonic circuits, supporting emerging applications in data communication, RF photonics, and quantum information systems[22].

 doi:10.20944/preprints202505.0911.v1

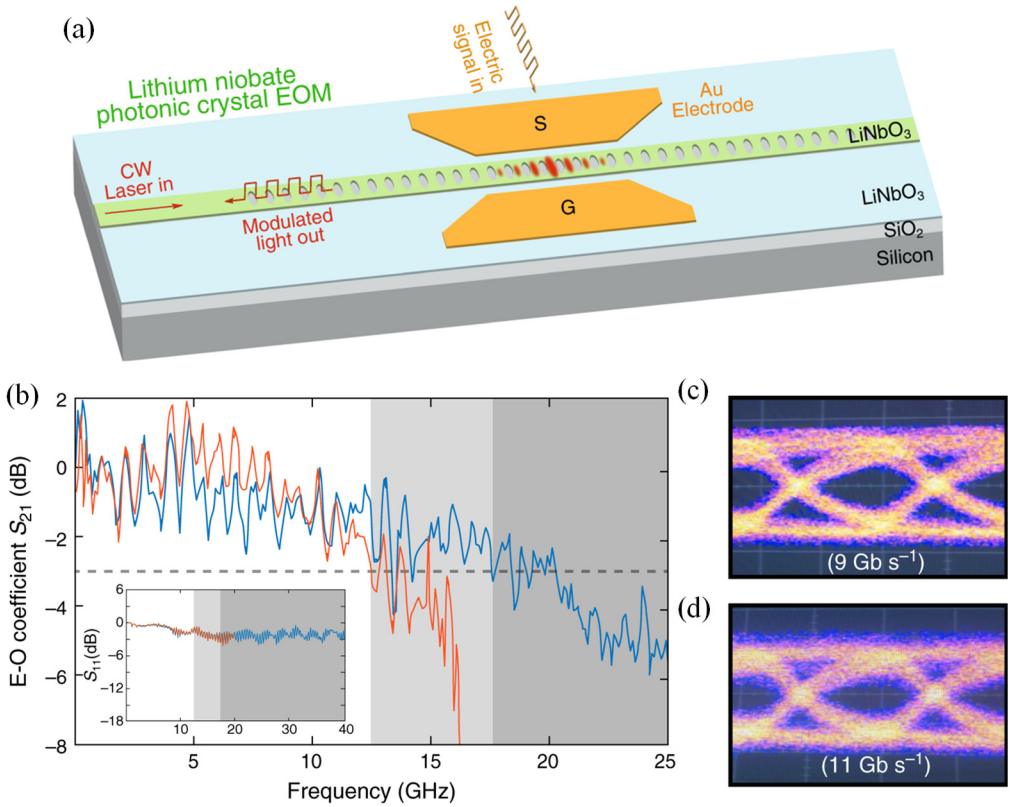

Figure 9. (a) Diagram of the LN photonic-crystal EO modulator, (b) Scattering parameter S21 for devices with optical Qs of ~14,000 (blue) and ~20,000 (orange). The gray regions represent the 3-dB bandwidth limits, and the dashed line indicates the 3-dB S_{21} limit. Inset: S_{11} reflection parameter for both devices, (c, d) Eye diagrams of the photonic-crystal EOM output, measured with a 2^7–1 NRZ PRBS and V_{pp} = 2 V, with the laser wavelength locked at the cavity resonance[22].

6.2. Insertion Loss, Bandwidth, and Speed

Insertion loss refers to the amount of optical power lost as light propagates through the tunable device[145,146]. Lower insertion loss is critical for high-performance photonic circuits to maintain signal integrity and minimize amplification requirements. EO modulators generally offer lower insertion loss compared to TO counterparts, largely due to the absence of heat-induced material absorption and scattering[147,148]. A new microheater design was introduced for efficient TO modulation in Si photonic platforms, utilizing indium tin oxide (ITO), a transparent, conductive material compatible with standard CMOS processes[149]. The design prioritized reducing the separation between the heater and waveguide to minimize optical losses. Performance analysis was carried out using finite element simulations, where ITO-based heaters were compared to traditional titanium heaters under different cladding conditions and for both TE and TM optical modes. Based on the simulation outcomes, ITO microheaters were fabricated with optimized structural parameters. Experimental validation showed that a heater with a length of 50 μm achieved a π phase shift using only 10 mW of electrical power and demonstrated response times in the microsecond range. These findings underscore ITO's effectiveness as a low-loss, high-performance heating element and highlight its potential for supporting the integration of dense phase shifter arrays in future PICs[149].

Bandwidth and speed are essential parameters for dynamic modulation and switching applications[150–153]. EO devices typically offer superior speed, often reaching tens of gigahertz due to the instantaneous nature of electric field modulation. In contrast, TO devices are inherently slower, with modulation speeds generally limited to the kilohertz range because of the thermal diffusion processes involved. However, their simplicity and ease of integration can offset these speed limitations in applications that do not require rapid reconfiguration.

 doi:10.20944/preprints202505.0911.v1

High-power tunable lasers are essential for applications such as telecommunications, sensing, and ranging. Integrated photonics has faced challenges in this area due to limited energy storage and low output power resulting from compact device sizes. In fiber optics, the introduction of large-mode-area fibers significantly improved power handling by expanding the optical mode, a concept that can also be applied at the chip level. Singh et al. introduced a Si photonics-based large mode area amplifier that enables a compact, high-power tunable laser[154]. The system delivered up to 1.8 watts of output across a tuning range of 60 nm, from 1.83 to 1.89 μm, constrained only by the seed laser source. Figure 10 (a) illustrates the experimental setup, where pump and seed lasers were coupled into the chip using a custom-built laser source tunable from 1830 to 1890 nm. Coupling losses were approximately 2.2 decibels for the pump and 2.4 decibels for the signal. Both copropagating and counterpropagating configurations yielded similar results, as the strong seed signal suppressed amplified spontaneous emission. Polarization remained consistent throughout the chip, with an extinction ratio exceeding 30 decibels. A six-centimeter device length provided the best performance. Figures 10 (b-e) show the amplified output power ranging from 1650 to 1800 milliwatts, achieving gains between 11.5 and 13.5 decibels. Even higher gains were observed but limited by facet reflection, which can be minimized through index matching or angled facets in future integrated designs.

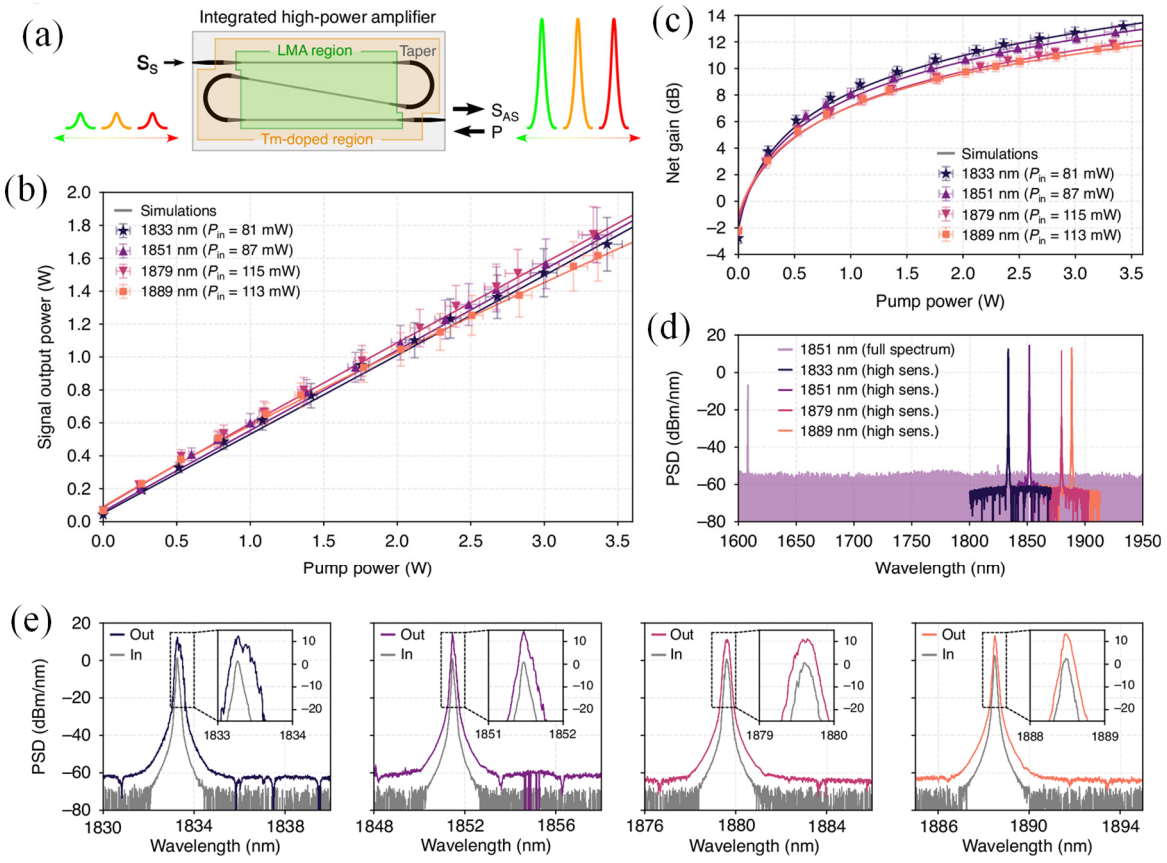

Figure 10. (a) Diagram of the counterpropagating setup where the pump enters from the opposite side of the seed laser. The seed is amplified using a large mode area amplifier, (b) Amplified output power as a function of pump input for seed wavelengths from 1830 to 1890 nm, with input powers between 81 and 115 milliwatts, (c) Net gain versus pump power, with error bars reflecting a 0.3 decibel coupling uncertainty, (d) Broadband output spectra show minimal ASE between pump and signal due to strong seed input, (e) Input and amplified output spectra across 1830 to 1890 nm, with observed gains of 10 to 12 decibels[154].

Figure 10 (d) presents the broad output spectrum extending to 1950 nm, free from amplified spontaneous emission background. Figure 10 (e) compares the input and output spectra, showing a high signal-to-noise ratio and minor broadening due to back-reflection, which can be addressed with proper output isolation. Longer devices of 11 cm to 15 cm showed slightly reduced gain at current

 doi:10.20944/preprints202505.0911.v1

pump levels but are expected to perform better under increased pump power. The system maintained stable operation over extended durations. This approach provided a significant power boost over conventional integrated tunable lasers, which typically operate in the milliwatt range. The results show performance comparable to or better than many benchtop systems, indicating strong potential for integrated high-power photonic solutions in practical applications[154].

6.3. Power Consumption

Power efficiency is another critical factor, particularly for large-scale PICs and portable devices[155–157]. TO tuning generally requires continuous power input to maintain elevated temperatures, resulting in higher steady-state power consumption. EO tuning, on the other hand, can be more energy-efficient since voltage application does not necessarily involve power dissipation if designed with capacitive actuation. For instance, Zhong et al. presented a Si EO switch based on photonic crystal nanobeam cavities, fabricated on a foundry-compatible platform[158]. The device featured ultra-low static tuning power (0.10 mW), low dynamic energy consumption (6.34 fJ/bit), and a compact footprint of 18 μm × 200 μm. High-speed performance was validated using a 136 Gb/s PAM-4 signal. This switch offered the lowest static power and highest data rate among its class, making it ideal for applications in optical computing, data center interconnects, neural networks, and reconfigurable photonics[158]. Nonetheless, the overall power budget also depends on drive circuitry, device geometry, and system-level thermal management strategies[156].

Scaling artificial intelligence (AI) systems require not only powerful computation but also efficient communication between distributed processing units. A significant bottleneck in this process is the high energy cost and chip area needed for transferring data across chips. To overcome this limitation, Daudlin et al. presented a novel solution based on dense three-dimensional (3D) integration of photonic and electronic components[155]. The photonic-electronic integration process for chip-to-chip communication is illustrated in Figure 11, which outlines each stage of the assembly in detail. The process begins with the formation of copper pillar bumps on the photonic chip. These structures are created through electroplating, where copper pedestals are topped with a thin tin layer. To complete the integration, the photonic chip was aligned with a nickel-coated electronic chip and bonded using heat and pressure (Figure 11 (a)). Following this, the result of the microbump fabrication is shown in the microscope image of the photonic device array (Figure 11 (b)). This array is embedded within a test photonic chip, which interfaces with a corresponding electronic test chip. Figure 11 (c) presents this setup alongside a schematic depicting how optical fibres coupled with the chip[155].

The bonding design includes 2,304 interconnects laid out with a tight pitch, 15 μm spacing, and 10 μm bump diameter, yielding a 25 μm pitch. This high-density layout required precise control to prevent issues such as tin overflow, which can lead to electrical shorts, and tin deficiency, which may weaken bond reliability. To evaluate the structural integrity of the bonds, cross-sectional SEM was used (Figure 11 (d)). The images confirm successful isolation between bonds, and mechanical testing shows the bonded chips withstand a separation force of 2.1 kg (114.9 MPa). Electrical modeling indicated each bond exhibits a low capacitance of just 10 fF. Figure 11 (e) showcases the complete transceiver assembly, which was mounted on a printed circuit board using wire bonds and aligned optically with a fibre array. A detailed layer-by-layer cross-section is shown in Figure 11 (f), illustrating the composition of the electronic and photonic chips, the bonding interface, and how connections are made to both the fibre and the board.

This configuration delivered a significantly higher density of 3D-integrated channels than previously demonstrated, enabling a total bandwidth of 800 Gb/s and an impressive spatial data rate of 5.3 Tb/s per mm². The system also achieved exceptional energy efficiency, with the transmitter and receiver front ends consuming only 50 femtojoules and 70 femtojoules per bit, respectively, while operating at 10 Gb/s per channel. Such performance was made possible through a design that was fully compatible with standard 300-mm CMOS foundry processes, ensuring scalability and manufacturability. By minimizing the energy and area required for inter-chip communication, this

 doi:10.20944/preprints202505.0911.v1

platform offers a practical and scalable pathway to eliminate bandwidth limitations in next-generation AI hardware[155].

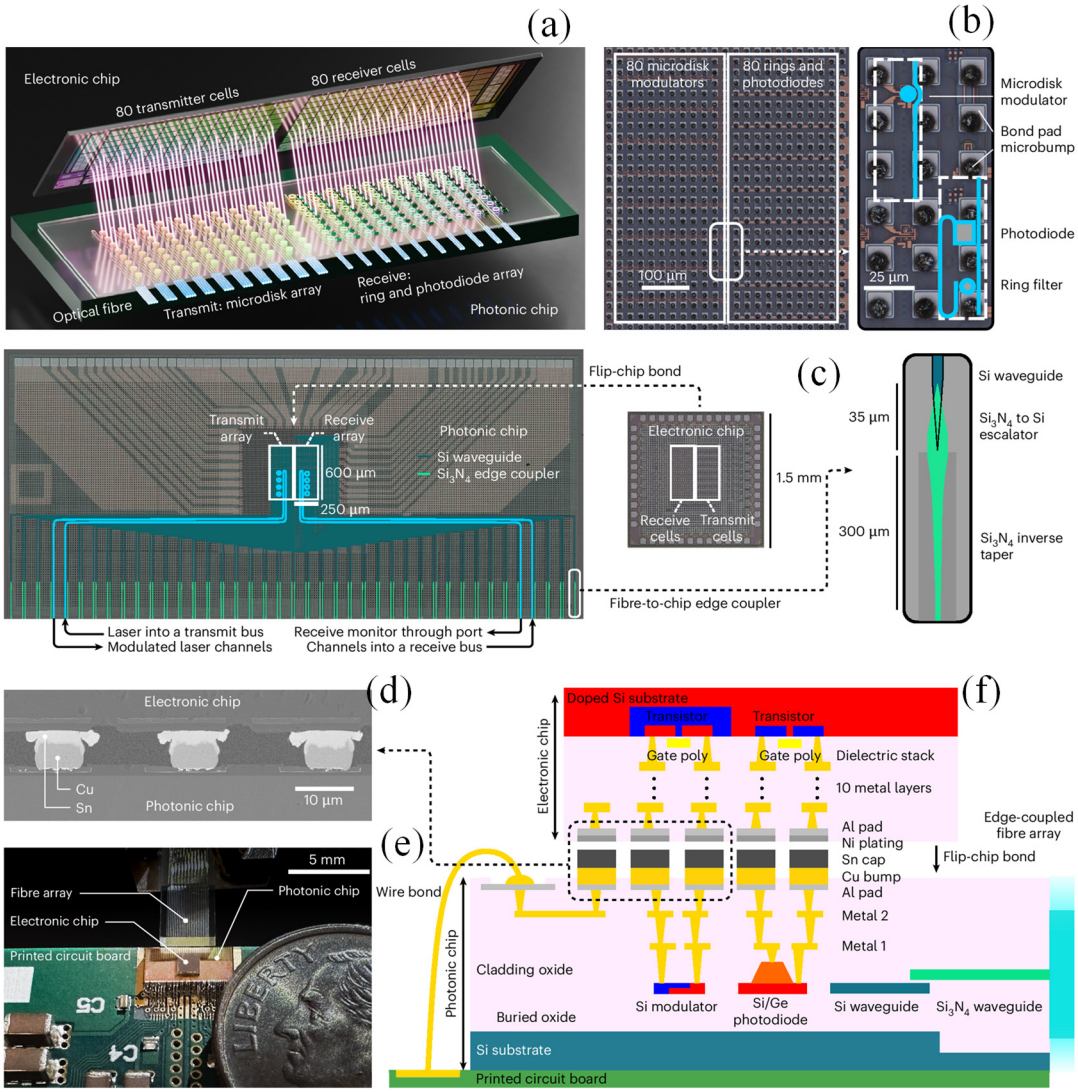

Figure 11. (a) Conceptual diagram of a vertically integrated system, aligning arrays of electronic circuits with corresponding photonic components, (b) Optical microscope image showing the 80-channel photonic array; inset highlights a pair of transmitter and receiver units, (c) Chip-level images of the photonic and electronic dies. The central, white-marked area contains active photonic circuits, while the surrounding region distributes optical and electrical connections for fiber and wire interfaces. A blue trace indicates a sample four-channel waveguide route. Inset: schematic of a fiber-to-chip coupler featuring a SiN taper transitioning into Si, (d) SEM cross-section capturing the bonded interface between the electronic and photonic layers, (e) Assembled transceiver module mounted on a printed circuit board and aligned to a fiber array, with a U.S. dime shown for size reference, (f) Layered view illustrating the chip stack materials, including Si bases, doped device layers, and metal interconnects for both the photonic and electronic components[155].

6.4. Long-Term Stability and Fatigue

Stability over time and resistance to fatigue are vital for ensuring the reliability of tunable photonic devices[159]. TO devices may suffer from material degradation and performance drift due to repeated heating and cooling cycles, which can affect polymer-based materials more significantly than crystalline semiconductors. EO materials such as LN and BTO exhibit better long-term EO stability and lower susceptibility to fatigue, though dielectric breakdown and charge trapping can pose reliability challenges if not properly mitigated. For both material classes, encapsulation

 doi:10.20944/preprints202505.0911.v1

techniques, thermal isolation structures, and robust packaging are essential to enhance operational longevity[160].

A novel optoelectronic oscillator (OEO) architecture based on stimulated Brillouin scattering was proposed, offering both high frequency stability and fine tunability[161]. Central to this design is the use of a single laser source to generate both the Brillouin pump and the optical carrier within the OEO loop. This shared-source approach ensures excellent coherence and stability in the resulting microwave signal. Fine frequency control was realized through an EO frequency shifter, which integrates a dual-parallel Mach–Zehnder modulator (DPMZM) with an electrical 90° hybrid coupler. By precisely adjusting the frequency of a low-frequency microwave signal applied to the DPMZM, the system enabled generation of a high-frequency microwave output with fine resolution. Experimental validation demonstrated a continuous tuning range from 10.645 GHz to 12.645 GHz, achieved with 10 MHz resolution. At a representative frequency of 11.145 GHz, the system exhibited minimal drift, with measured frequency and power fluctuations limited to 6.25 kHz and 0.77 dB, respectively, over a 1000-second interval. Moreover, by incorporating broadband optical and electrical components, the proposed OEO configuration was scalable and capable of supporting stable microwave signal generation up to 40 GHz or higher, making it suitable for a wide range of high-frequency applications[161].

EO polymer modulators with high thermal stability are increasingly in demand for advanced photonic applications. In response, Miura et al. developed a series of EO polymers exhibiting glass transition temperatures as high as 194°C[159]. These materials were integrated into MZI modulators, which demonstrated exceptional thermal endurance. Specifically, the modulators maintained stable half-wave voltage performance during continuous operation at 105°C for approximately 2,000 hours. To further evaluate their performance under thermal stress, the modulators were equipped with traveling-wave electrodes and tested across the 10–40 GHz frequency range as the operating temperature increased. The results revealed a consistently reliable frequency response, with modulation capabilities sustained up to 130°C. These findings confirm the effectiveness of the developed EO polymers in supporting high-frequency, thermally robust modulators suitable for demanding environments[159].

Kieninger et al. demonstrated Si-organic hybrid (SOH) modulators that maintain long-term thermal stability, meeting Telcordia reliability standards for high-temperature operation[162]. These devices incorporated an organic EO polymer with a glass transition temperature of 172 °C. Figure 12 (a,b) illustrates the structure of an SOH Mach-Zehnder modulator (MZM). In Figure 12 (a), the top view shows two multi-mode interference (MMI) couplers used to split and recombine the optical signal. The modulator integrates a ground-signal-ground (GSG) coplanar transmission line for driving the radio frequency (RF) signal across the device. Figure 12 (b) presents a perspective view of the MZM arms, each composed of a Si slot waveguide formed by two closely spaced rails filled with an organic electro-optic (OEO) material. Thin n-doped Si slabs and electrical vias connect the slot waveguides to the aluminum GSG electrodes. The RF drive voltage was concentrated across the narrow slot, generating strong electric fields in the OEO region. This, combined with the confinement of the optical mode in the same slot, results in a high modulation efficiency. EO activity was established through a one-time poling process, where the device was heated near the glass transition temperature of the OEO material, and a voltage is applied to align dipolar molecules. Once cooled, this alignment is fixed, allowing push-pull operation via differential phase shifts in the two arms of the modulator.

The experimental setup is shown in Figure 12 (c). OOK eye diagrams at 40 Gbit/s for Device 5 (330 h) and Device 2 (2700 h) show a π-voltage increase from 2.0 V to 2.2 V (Figure 12 (d)). To maintain similar signal quality, Device 5 was driven at 1.7 Vpp (Q factor = 8.9), while Device 2 required 1.9 Vpp (Q factor = 8.3). The 10% increase in drive voltage corresponds to the higher π-voltage of Device 2, indicating that high-temperature storage primarily affects π-voltage without altering high-speed performance. The modulators continue to deliver high-performance operation, as confirmed by the generation of 40 Gbit/s on-off keying signals after both burn-in and long-term thermal storage[162].

 doi:10.20944/preprints202505.0911.v1

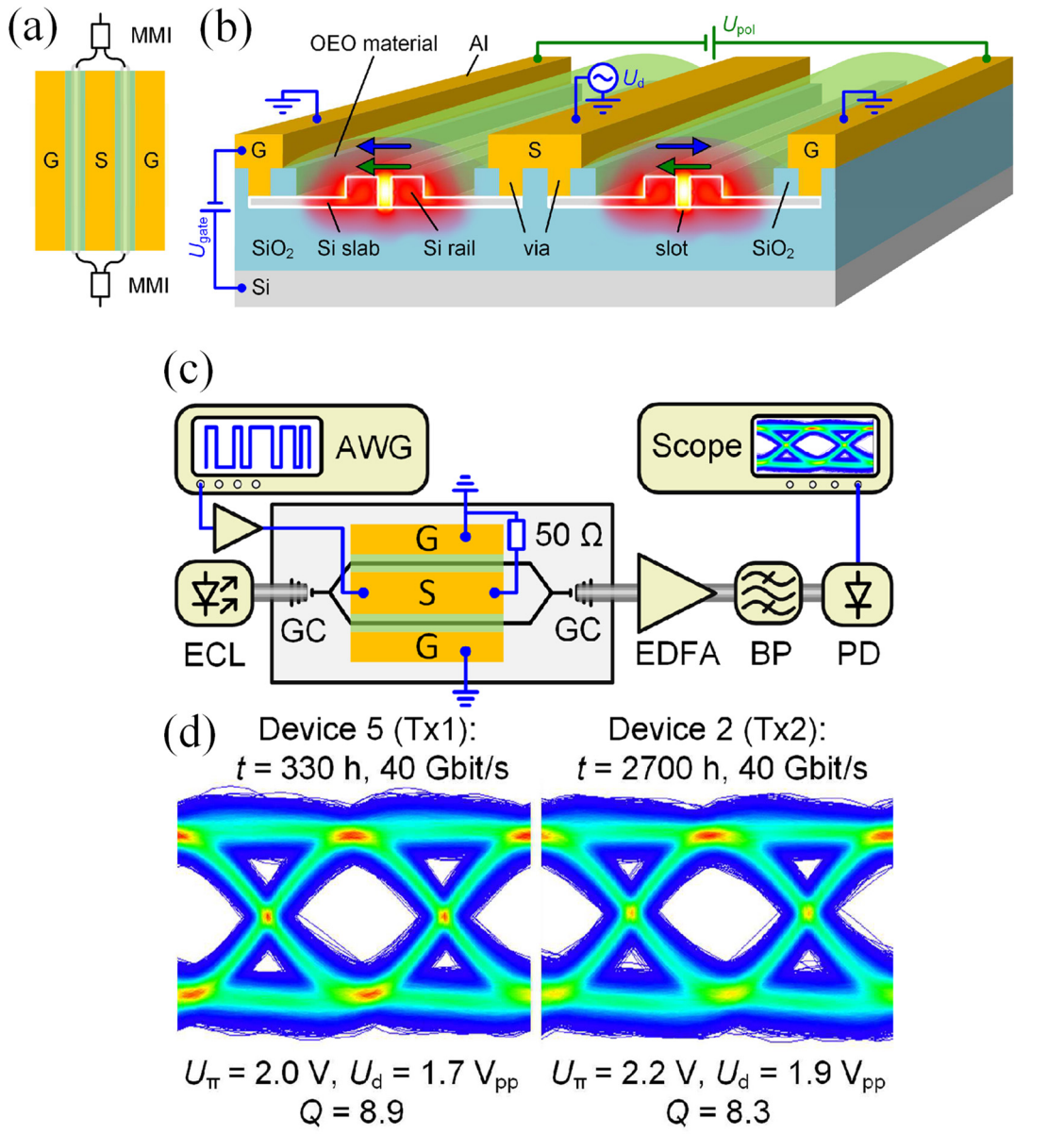

Figure 12. SOH MZM and data transmission: (a) Top view of the SOH modulator showing the ground-signal-ground transmission line and multi-mode interference couplers, (b) Perspective view illustrating Si slot waveguides filled with EO material, with strong RF and optical mode overlap in the slot. EO activity is set via thermal poling and retained upon cooling; applied signal voltages enable push-pull modulation, (c) Setup for 40 Gbit/s data transmission using an amplified electrical signal and optical carrier, with digital filtering at the receiver, (d) Eye diagrams for Device 5 after 330 h and Device 2 after 2700 h high-temperature storage show minimal signal degradation; Device 2 requires ~10% higher drive voltage[162].

7. Emerging Trends and Future Directions

The field of TO and EO materials is experiencing a paradigm shift, driven by the increasing demand for highly integrated, energy-efficient, and dynamically reconfigurable photonic systems. A prominent trajectory in current research is the integration of functional tunable materials with Si photonics and PICs[163]. While Si offers a well-established, CMOS-compatible platform with high fabrication maturity, its inherently weak EO and TO coefficients limit its utility in actively tunable applications[164]. To address this limitation, significant efforts have been directed toward the heterogeneous or hybrid integration of materials exhibiting strong Pockels or TO effects, such as LN[54,87,165], BTO[166,167], and EO polymers[168,169] onto Si substrates. This approach enables the realization of high-speed modulators, low-power switches, and thermally reconfigurable waveguide

 doi:10.20944/preprints202505.0911.v1

components. Recent progress in wafer bonding[170,171], thin-film deposition[172], and patterning techniques[173–175] have facilitated the development of monolithically integrated photonic circuits with enhanced tunability, bandwidth, and operational stability[86].

Concurrently, the application of artificial intelligence (AI) and machine learning (ML) methodologies is revolutionizing the discovery and optimization of tunable photonic materials[176,177]. Data-driven approaches and high-throughput screening, combined with inverse design algorithms, enable the prediction and tailoring of key material parameters such as refractive index modulation, EOCs, dielectric breakdown strength, and thermal conductivity across vast compositional spaces[178]. These techniques not only accelerate the identification of novel materials with targeted performance metrics but also support the optimization of synthesis and processing conditions. Furthermore, AI-assisted process control during fabrication emerges as a powerful tool for minimizing variability, enhancing yield, and enabling adaptive tuning in complex photonic architectures[179,180].

Another critical direction involves the development of materials that exhibit high environmental stability and low energy consumption. Many conventional tunable materials, including liquid crystals and phase-change compounds, suffer from limitations such as thermal instability, volatility, and elevated switching thresholds[181,182]. Consequently, recent research has focused on engineering new classes of hybrid organic-inorganic materials, doped polymers, and chemically stabilized perovskites that exhibit robust performance under ambient environmental conditions. These materials are designed to retain tunability while minimizing power consumption and ensuring long-term operational reliability[183]. This is particularly crucial for emerging applications in portable and wearable photonics, remote sensing, and distributed optical systems, where energy efficiency and environmental resilience are essential[184].

In parallel, the advent of additive manufacturing techniques, including multi-material 3D printing, has opened new pathways for fabricating complex, lightweight, and flexible photonic structures incorporating tunable materials[185,186]. The ability to deposit functional materials with precise spatial control enables the construction of conformal and non-planar photonic elements, which are essential for applications in soft robotics, biomedical devices, and embedded optical systems. Moreover, the incorporation of EO and TO materials into printable inks has facilitated the development of reconfigurable photonic circuits and devices with spatially localized tuning capabilities. These developments represent a significant step toward customizable, low-cost, and scalable manufacturing of integrated photonic systems.

The application landscape for tunable photonic materials continues to expand, encompassing domains such as light detection and ranging (LiDAR), neuromorphic photonics, and quantum information processing[187,188]. In LiDAR, solid-state beam steering using tunable photonic components enables high-speed, vibration-resistant systems with improved resolution and field-of-view. In neuromorphic computing, EO materials with nonlinear and memory-like behavior are being employed to emulate synaptic functionalities in photonic neural networks, offering pathways toward ultra-fast, low-power computation[189]. In the context of quantum photonics, materials capable of precise and rapid refractive index modulation are critical for the realization of tunable quantum gates, on-demand photon sources, and dynamically reconfigurable quantum circuits[190]. As these emerging applications impose increasingly stringent requirements on material performance, the continued development of advanced tunable materials will play a pivotal role in the future of photonic technologies.

8. Final Remarks

TO and EO materials have emerged as essential building blocks for tunable photonic devices, enabling dynamic modulation and control of optical signals across a broad spectrum of applications. These materials underpin a wide range of technologies, including optical switches, modulators, filters, sensors, and reconfigurable waveguides, which are foundational to telecommunications, data centers, biomedical imaging, and emerging quantum photonic systems. TO materials offer the

 doi:10.20944/preprints202505.0911.v1

advantages of simplicity, compatibility with various platforms, including Si and polymer photonics, and ease of fabrication. However, their reliance on thermal diffusion inherently limits their speed and energy efficiency. Despite these challenges, they remain indispensable in scenarios where modulation bandwidth is secondary to fabrication scalability and cost-effectiveness.

EO materials, particularly those exhibiting the Pockels effect, provide ultrafast response times and high-precision refractive index control, making them ideal for high-frequency signal processing and advanced modulation formats. Materials such as LN, BTO, and certain organic chromophores are at the forefront of these developments. Nevertheless, challenges persist in achieving low-voltage operation, stable long-term performance, and compatibility with complementary metal oxide semiconductor fabrication processes. A key trend in the field is the growing interest in hybrid integration, where multiple materials and tuning mechanisms are combined to optimize performance across multiple metrics. For instance, incorporating PCMs, two-dimensional semiconductors, or nanostructured metamaterials can offer nonvolatile tuning, enhanced confinement, and novel nonlinear responses. Furthermore, the integration of AI and ML algorithms with photonic circuits may enable smarter, adaptive tuning and system-level optimization.

Future progress will depend on addressing several critical challenges: developing low-loss and CMOS-compatible materials, improving the stability and repeatability of tuning responses, and ensuring scalable fabrication for commercial deployment. Research into novel material systems, such as lead-free perovskites, graphene-based composites, and topological photonic materials, holds significant promise in overcoming existing tradeoffs between speed, power consumption, and integration complexity.

To conclude, the convergence of TO and EO technologies, supported by interdisciplinary advances in material science, nanofabrication, and device engineering, is paving the way for the next generation of agile and programmable photonic systems. These technologies will be central to the realization of intelligent optical networks, compact lab-on-chip systems, and scalable quantum photonic architectures. Continued innovation and collaboration across academic, industrial, and governmental research sectors will be vital to unlocking the full potential of tunable photonic devices in the years ahead.

Funding: This research received no external funding.

Institutional Review Board Statement: Not applicable.

Informed Consent Statement: Not applicable.

Data Availability Statement: No new data was created.

Acknowledgments: The author acknowledges the constant support of the Warsaw University of Technology in the completion of this work.

Conflicts of Interest: The authors declare no conflicts of interest.

Abbreviations

Thermo-optic=TO; Electro-optic=EO, Lithium niobate=LN; Silicon=Si; Silicon nitride=SiN; Thermo-optic coefficient=TOC; Electro-optic coefficient=EOC; Phase change material=PCM; Barium Titanate=BTO; Complementary metal-oxide semiconductor=CMOS; Mach-Zehnder interferometer=MZI; Microring resonator=MRR; Photonic integrated circuit=PIC; Metasurfaces=MS.

 doi:10.20944/preprints202505.0911.v1

References

1. Chrostowski, L.; Grist, S.; Flueckiger, J.; Shi, W.; Wang, X.; Ouellet, E.; Yun, H.; Webb, M.; Nie, B.; Liang, Z.; et al. Silicon Photonic Resonator Sensors and Devices. In Proceedings of the Laser Resonators, Microresonators, and Beam Control XIV; SPIE, February 6 2012; Vol. 8236, pp. 387–402.
2. Altug, H.; Oh, S.-H.; Maier, S.A.; Homola, J. Advances and Applications of Nanophotonic Biosensors. *Nat. Nanotechnol.* **2022**, *17*, 5–16, doi:10.1038/s41565-021-01045-5.
3. Cao, Z.; He, J.-J.; Guo, Y.; Li, M. Optical Ring Resonator Biosensor for Small Molecule Detection. In Proceedings of the Asia Communications and Photonics Conference (2017), paper S4I.5; Optica Publishing Group, November 10 2017; p. S4I.5.
4. Butt, M.A. A Comprehensive Exploration of Contemporary Photonic Devices in Space Exploration: A Review. *Photonics* **2024**, *11*, 873, doi:10.3390/photonics11090873.
5. Ko, J.H.; Yoo, Y.J.; Lee, Y.; Jeong, H.-H.; Song, Y.M. A Review of Tunable Photonics: Optically Active Materials and Applications from Visible to Terahertz. *iScience* **2022**, *25*, 104727, doi:10.1016/j.isci.2022.104727.
6. Woska, S.; Münchinger, A.; Beutel, D.; Blasco, E.; Hessenauer, J.; Karayel, O.; Rietz, P.; Pfleging, S.; Oberle, R.; Rockstuhl, C.; et al. Tunable Photonic Devices by 3D Laser Printing of Liquid Crystal Elastomers. *Opt. Mater. Express, OME* **2020**, *10*, 2928–2943, doi:10.1364/OME.402855.
7. Afridi, A.; Gieseler, J.; Meyer, N.; Quidant, R. Ultrathin Tunable Optomechanical Metalens. *Nano Lett.* **2023**, *23*, 2496–2501, doi:10.1021/acs.nanolett.2c04105.
8. Effah, E.; Nettey-Oppong, E.E.; Ali, A.; Byun, K.M.; Choi, S.H. Tunable Metasurfaces Based on Mechanically Deformable Polymeric Substrates. *Photonics* **2023**, *10*, 119, doi:10.3390/photonics10020119.
9. Arbabi, E.; Arbabi, A.; Kamali, S.M.; Horie, Y.; Faraji-Dana, M.; Faraon, A. MEMS-Tunable Dielectric Metasurface Lens. *Nat Commun* **2018**, *9*, 812, doi:10.1038/s41467-018-03155-6.
10. Bai, W.; Yang, P.; Huang, J.; Chen, D.; Zhang, J.; Zhang, Z.; Yang, J.; Xu, B. Near-Infrared Tunable Metalens Based on Phase Change Material Ge2Sb2Te5. *Sci Rep* **2019**, *9*, 5368, doi:10.1038/s41598-019-41859-x.
11. Shalaginov, M.Y.; An, S.; Zhang, Y.; Yang, F.; Su, P.; Liberman, V.; Chou, J.B.; Roberts, C.M.; Kang, M.; Rios, C.; et al. Reconfigurable All-Dielectric Metalens with Diffraction-Limited Performance. *Nat Commun* **2021**, *12*, 1225, doi:10.1038/s41467-021-21440-9.
12. Ghaffari, V.; Yousefi, L. Integrated Optical Beam Steering Device Using Switchable Nanoantennas and a Reflective Metalens. *Sci Rep* **2023**, *13*, 7099, doi:10.1038/s41598-023-33939-w.
13. Guarino, A.; Poberaj, G.; Rezzonico, D.; Degl'Innocenti, R.; Günter, P. Electro–Optically Tunable Microring Resonators in Lithium Niobate. *Nature Photon* **2007**, *1*, 407–410, doi:10.1038/nphoton.2007.93.
14. Ceccarelli, F.; Rakonjac, J.V.; Grandi, S.; Riedmatten, H. de; Osellame, R.; Corrielli, G. Integrated Thermo-Optic Phase Shifters for Laser-Written Photonic Circuits Operating at Cryogenic Temperatures. *J. Phys. Photonics* **2024**, *6*, 045023, doi:10.1088/2515-7647/ad82c2.
15. Iyer, P.P.; DeCrescent, R.A.; Lewi, T.; Antonellis, N.; Schuller, J.A. Uniform Thermo-Optic Tunability of Dielectric Metalenses. *Phys. Rev. Appl.* **2018**, *10*, 044029, doi:10.1103/PhysRevApplied.10.044029.
16. Juan-Colás, J.; Johnson, S.; Krauss, T.F. Dual-Mode Electro-Optical Techniques for Biosensing Applications: A Review. *Sensors* **2017**, *17*, 2047, doi:10.3390/s17092047.
17. Wu, K.; Wang, Y.; Qiu, C.; Chen, J. Thermo-Optic All-Optical Devices Based on Two-Dimensional Materials. *Photon. Res., PRJ* **2018**, *6*, C22–C28, doi:10.1364/PRJ.6.000C22.
18. Karimi, Y.; Kaatuzian, H. Low-Power Fano Resonance-Based MIM Plasmonic Switch Using Kerr-Type Nonlinear Material. In Proceedings of the 2021 29th Iranian Conference on Electrical Engineering (ICEE); May 2021; pp. 32–35.
19. Li, M.; Tang, H.X. Strong Pockels Materials. *Nature Mater* **2019**, *18*, 9–11, doi:10.1038/s41563-018-0259-2.
20. Yadav, A.; Kumar, A.; Prakash, A. Design and Analysis of Optical Switches Using Electro-Optic Effect Based Mach-Zehnder Interferometer Structures. *Materials Today: Proceedings* **2022**, *56*, 462–467, doi:10.1016/j.matpr.2022.01.454.
21. Sun, D. A Proposal for Digital Electro-Optic Switches with Free-Carrier Dispersion Effect and Goos-Hanchen Shift in Silicon-on-Insulator Waveguide Corner Mirror. *Journal of Applied Physics* **2013**, *114*, 104502, doi:10.1063/1.4820378.

 doi:10.20944/preprints202505.0911.v1

22. Li, M.; Ling, J.; He, Y.; Javid, U.A.; Xue, S.; Lin, Q. Lithium Niobate Photonic-Crystal Electro-Optic Modulator. *Nat Commun* **2020**, *11*, 4123, doi:10.1038/s41467-020-17950-7.
23. Aisheh, M.A.; Kalliyadan, A.C.; Abutoama, M.; Abuleil, M.J.; Abdulhalim, I. Deep Gratings Filled with Liquid Crystal as Tunable Photonic Metamaterial. In Proceedings of the Liquid Crystals Optics and Photonic Devices; SPIE, June 18 2024; Vol. 13016, p. 1301602.
24. Bennet, M.; Gur, D.; Yoon, J.; Park, Y.; Faivre, D. A Bacteria-Based Remotely Tunable Photonic Device. *Advanced Optical Materials* **2017**, *5*, 1600617, doi:10.1002/adom.201600617.
25. Muñoz-Hernández, T.; Reyes-Vera, E.; Torres, P. Tunable Whispering Gallery Mode Photonic Device Based on Microstructured Optical Fiber with Internal Electrodes. *Sci Rep* **2019**, *9*, 12083, doi:10.1038/s41598-019-48598-z.
26. Wu, Q.; Zhang, H.; Jia, D.; Liu, T. Recent Development of Tunable Optical Devices Based on Liquid. *Molecules* **2022**, *27*, 8025, doi:10.3390/molecules27228025.
27. Asquini, R.; d'Alessandro, A. Tunable Photonic Devices Based on Liquid Crystals and Composites. In Proceedings of the Liquid Crystals XVII; SPIE, September 12 2013; Vol. 8828, pp. 108–121.
28. Chapter 3 - Thermo-Optic Coefficients. In *Handbook of Optical Constants of Solids*; Palik, E.D., Ed.; Academic Press: Burlington, 1997; pp. 115–261 ISBN 978-0-12-544415-6.
29. Hu, J.; Wu, J.; Liu, W.; Jin, D.; Dirani, H.E.; Kerdiles, S.; Sciancalepore, C.; Demongodin, P.; Grillet, C.; Monat, C.; et al. 2D Graphene Oxide: A Versatile Thermo-Optic Material. *Advanced Functional Materials* **2024**, *34*, 2406799, doi:10.1002/adfm.202406799.
30. Xie, Y.; Chen, L.; Li, H.; Yi, Y. Polymer and Hybrid Optical Devices Manipulated by the Thermo-Optic Effect. *Polymers* **2023**, *15*, 3721, doi:10.3390/polym15183721.
31. Allen, S. Electro-Optic Materials and Applications. In *Electronic Materials: From Silicon to Organics*; Miller, L.S., Mullin, J.B., Eds.; Springer US: Boston, MA, 1991; pp. 301–313 ISBN 978-1-4615-3818-9.
32. Feng, S.; Wu, S.; Zhang, W.; Liu, F.; Wang, J. Organic Electro-Optic Materials with High Electro-Optic Coefficients and Strong Stability. *Molecules* **2024**, *29*, 3188, doi:10.3390/molecules29133188.
33. Dushaq, G.; Serunjogi, S.; Tamalampudi, S.R.; Rasras, M. Electro-Optic Tuning in Composite Silicon Photonics Based on Ferroionic 2D Materials. *Light Sci Appl* **2024**, *13*, 92, doi:10.1038/s41377-024-01432-2.
34. Chu, T.; Yamada, H.; Ishida, S.; Arakawa, Y. Compact 1 × N Thermo-Optic Switches Based on Silicon Photonic Wire Waveguides. *Opt. Express, OE* **2005**, *13*, 10109–10114, doi:10.1364/OPEX.13.010109.
35. Butt, M.A. High Sensitivity Design for Silicon-On-Insulator-Based Asymmetric Loop-Terminated Mach-Zehnder Interferometer. *Materials 18*, 798.
36. Bose, D.; Harrington, M.W.; Isichenko, A.; Liu, K.; Wang, J.; Chauhan, N.; Newman, Z.L.; Blumenthal, D.J. Anneal-Free Ultra-Low Loss Silicon Nitride Integrated Photonics. *Light Sci Appl* **2024**, *13*, 156, doi:10.1038/s41377-024-01503-4.
37. Zabelich, B.; Nitiss, E.; Stroganov, A.; Brès, C.-S. Linear Electro-Optic Effect in Silicon Nitride Waveguides Enabled by Electric-Field Poling. *ACS Photonics* **2022**, *9*, 3374–3383, doi:10.1021/acsphotonics.2c00888.
38. Yu, T.-C.; Liu, A.-C.; Huang, W.-T.; Wu, C.-C.; Li, C.-H.; Kao, T.-S.; Chang, S.-W.; Sher, C.-W.; Lin, H.-Y.; Chow, C.-W.; et al. Comparison of Thin-Film Lithium Niobate, SOH, and POH for Silicon Photonic Modulators. *Photonics* **2025**, *12*, 429, doi:10.3390/photonics12050429.
39. Lee, Y.H.; Park, S.; Won, Y.; Mun, J.; Ha, J.H.; Lee, J.H.; Lee, S.H.; Park, J.; Yeom, J.; Rho, J.; et al. Flexible High-Performance Graphene Hybrid Photodetectors Functionalized with Gold Nanostars and Perovskites. *NPG Asia Mater* **2020**, *12*, 1–12, doi:10.1038/s41427-020-00260-1.
40. Abbas, K.; Ji, P.; Ullah, N.; Shafique, S.; Zhang, Z.; Ameer, M.F.; Qin, S.; Yang, S. Graphene Photodetectors Integrated with Silicon and Perovskite Quantum Dots. *Microsyst Nanoeng* **2024**, *10*, 1–13, doi:10.1038/s41378-024-00722-4.
41. Li, W.; et al. Infrared Light Emission Devices Based on Two-Dimensional Materials. *Nanomaterials* **2022**, *12*, 2996.
42. Sherawat, V.; Bokolia, R.; Sinha, R.K. Impact of Thermal and Refractive Index Tuning on the Bandgap and Band-Edges of a Silicon Photonic Crystal Waveguide with Sensing Applications. *Optics Communications* **2022**, *518*, 128348, doi:10.1016/j.optcom.2022.128348.

 doi:10.20944/preprints202505.0911.v1

43. Pant, B.; Zhang, W.; Ebert, M.; Yan, X.; Du, H.; Banakar, M.; Tran, D.T.; Qi, Y.; Rowe, D.; Jeyaselvan, V.; et al. Study into the Spread of Heat from Thermo-Optic Silicon Photonic Elements. *Opt. Express, OE* **2021**, *29*, 36461–36468, doi:10.1364/OE.426748.
44. Rao, S.; Mallemace, E.D.; Faggio, G.; Iodice, M.; Messina, G.; Della Corte, F.G. Experimental Characterization of the Thermo-Optic Coefficient vs. Temperature for 4H-SiC and GaN Semiconductors at the Wavelength of 632 Nm. *Sci Rep* **2023**, *13*, 10205, doi:10.1038/s41598-023-37199-6.
45. Komma, J.; Schwarz, C.; Hofmann, G.; Heinert, D.; Nawrodt, R. Thermo-Optic Coefficient of Silicon at 1550 Nm and Cryogenic Temperatures. *Applied Physics Letters* **2012**, *101*, 041905, doi:10.1063/1.4738989.
46. Bednarski, H.; Hajduk, B. Dispersion of Thermo-Optic Coefficient of Optical Polymers. *Polymer* **2021**, *230*, 124074, doi:10.1016/j.polymer.2021.124074.
47. Fang, Y.; Furniss, D.; Jayasuriya, D.; Parnell, H.; Tang, Z.; Seddon, A.B.; Benson, T.M. Determining the Continuous Thermo-Optic Coefficients of Chalcogenide Glass Thin Films in the MIR Region Using FTIR Transmission Spectra. *Opt. Express, OE* **2019**, *27*, 22275–22288, doi:10.1364/OE.27.022275.
48. Lee, M.W.; Grillet, C.; Monat, C.; Mägi, E.; Tomljenovic-Hanic, S.; Gai, X.; Madden, S.; Choi, D.-Y.; Bulla, D.; Luther-Davies, B.; et al. Photosensitive and Thermal Nonlinear Effects in Chalcogenide Photonic Crystal Cavities. *Opt. Express, OE* **2010**, *18*, 26695–26703, doi:10.1364/OE.18.026695.
49. Gan, S.; Cheng, C.; Zhan, Y.; Huang, B.; Gan, X.; Li, S.; Lin, S.; Li, X.; Zhao, J.; Chen, H.; et al. A Highly Efficient Thermo-Optic Microring Modulator Assisted by Graphene. *Nanoscale* **2015**, *7*, 20249–20255, doi:10.1039/C5NR05084G.
50. Gutiérrez, Y.; Ovvyan, A.P.; Santos, G.; Juan, D.; Rosales, S.A.; Junquera, J.; García-Fernández, P.; Dicorato, S.; Giangregorio, M.M.; Dilonardo, E.; et al. Interlaboratory Study on Sb2S3 Interplay between Structure, Dielectric Function, and Amorphous-to-Crystalline Phase Change for Photonics. *iScience* **2022**, *25*, 104377, doi:10.1016/j.isci.2022.104377.
51. Ilie, S.T.; Faneca, J.; Zeimpekis, I.; Bucio, T.D.; Grabska, K.; Hewak, D.W.; Chong, H.M.H.; Gardes, F.Y. Thermo-Optic Tuning of Silicon Nitride Microring Resonators with Low Loss Non-Volatile $$\hbox {Sb}_{2}\hbox {S}_{3}$$ Phase Change Material. *Sci Rep* **2022**, *12*, 17815, doi:10.1038/s41598-022-21590-w.
52. Kim, I.; Demkov, A.A. Linear Electro-Optic Effect in Trigonal $\mathrm{LiNb}{\mathrm{O}}_{3}$: A First-Principles Study. *Phys. Rev. Mater.* **2024**, *8*, 025202, doi:10.1103/PhysRevMaterials.8.025202.
53. Vasudevan, A.T.; Selvaraja, S.K. Domain Effects on the Electro-Optic Properties of Thin-Film Barium Titanate. *Opt. Mater. Express, OME* **2023**, *13*, 956–965, doi:10.1364/OME.484836.
54. Chen, G.; Chen, K.; Gan, R.; Ruan, Z.; Wang, Z.; Huang, P.; Lu, C.; Lau, A.P.T.; Dai, D.; Guo, C.; et al. High Performance Thin-Film Lithium Niobate Modulator on a Silicon Substrate Using Periodic Capacitively Loaded Traveling-Wave Electrode. *APL Photonics* **2022**, *7*, 026103, doi:10.1063/5.0077232.
55. Peltier, J.; Zhang, W.; Virot, L.; Lafforgue, C.; Deniel, L.; Marris-Morini, D.; Aubin, G.; Amar, F.; Tran, D.; Yan, X.; et al. High-Speed Silicon Photonic Electro-Optic Kerr Modulation. *Photon. Res., PRJ* **2024**, *12*, 51–60, doi:10.1364/PRJ.488867.
56. Chelladurai, D.; Kohli, M.; Winiger, J.; Moor, D.; Messner, A.; Fedoryshyn, Y.; Eleraky, M.; Liu, Y.; Wang, H.; Leuthold, J. Barium Titanate and Lithium Niobate Permittivity and Pockels Coefficients from Megahertz to Sub-Terahertz Frequencies. *Nat. Mater.* **2025**, 1–8, doi:10.1038/s41563-025-02158-1.
57. Goodson, T., III; Wang, C.H. Quadratic Electro-absorption and Electro-optic Effects in a Guest/Host Nonlinear Optical Polymeric System. *Journal of Applied Physics* **1996**, *79*, 1267–1274, doi:10.1063/1.361021.
58. Shen, H.; Dutta, M. Franz–Keldysh Oscillations in Modulation Spectroscopy. *Journal of Applied Physics* **1995**, *78*, 2151–2176, doi:10.1063/1.360131.
59. Hu, Y.; Menyuk, C.R.; Hutchinson, M.N.; Urick, V.J.; Williams, K.J. Impact of the Coulomb Interaction on the Franz–Keldysh Effect in High-Current Photodetectors. *Opt. Lett., OL* **2016**, *41*, 456–459, doi:10.1364/OL.41.000456.
60. Ma, Z.; Li, Z.; Liu, K.; Ye, C.; Sorger, V.J. Indium-Tin-Oxide for High-Performance Electro-Optic Modulation. *Nanophotonics* **2015**, *4*, 198–213, doi:10.1515/nanoph-2015-0006.
61. Babicheva, V.E.; Boltasseva, A.; Lavrinenko, A.V. Transparent Conducting Oxides for Electro-Optical Plasmonic Modulators. *Nanophotonics* **2015**, *4*, 165–185, doi:10.1515/nanoph-2015-0004.

 doi:10.20944/preprints202505.0911.v1

62. Sinatkas, G.; Skandalos, I.; Christopoulos, T.; Kriezis, E.E. Electro-Optic Phase Modulators Based on Transparent-Conducting-Oxide Loaded Silicon Waveguides. In Proceedings of the 2017 IEEE 14th International Conference on Group IV Photonics (GFP); August 2017; pp. 147–148.
63. Sun, P.; Reano, R.M. Submilliwatt Thermo-Optic Switches Using Free-Standing Silicon-on-Insulator Strip Waveguides. *Opt. Express, OE* **2010**, *18*, 8406–8411, doi:10.1364/OE.18.008406.
64. Cui, Y.; Liu, K.; MacFarlane, D.L.; Lee, J.-B. Thermo-Optically Tunable Silicon Photonic Crystal Light Modulator. *Opt. Lett., OL* **2010**, *35*, 3613–3615, doi:10.1364/OL.35.003613.
65. Ding, Y.; Tao, S.; Wang, X.; Shang, C.; Pan, A.; Zeng, C.; Xia, J. Thermo-Optic Tunable Optical Filters with GHz-Bandwidth and Flat-Top Passband on Thin Film Lithium Niobate Platform. *Opt. Express, OE* **2022**, *30*, 22135–22142, doi:10.1364/OE.458218.
66. Harris, N.C.; Ma, Y.; Mower, J.; Baehr-Jones, T.; Englund, D.; Hochberg, M.; Galland, C. Efficient, Compact and Low Loss Thermo-Optic Phase Shifter in Silicon. *Opt. Express, OE* **2014**, *22*, 10487–10493, doi:10.1364/OE.22.010487.
67. Liu, S.; Feng, J.; Tian, Y.; Zhao, H.; Jin, L.; Ouyang, B.; Zhu, J.; Guo, J. Thermo-Optic Phase Shifters Based on Silicon-on-Insulator Platform: State-of-the-Art and a Review. *Front. Optoelectron.* **2022**, *15*, 9, doi:10.1007/s12200-022-00012-9.
68. Gan, F.; Barwicz, T.; Popovic, M.A.; Dahlem, M.S.; Holzwarth, C.W.; Rakich, P.T.; Smith, H.I.; Ippen, E.P.; Kartner, F.X. Maximizing the Thermo-Optic Tuning Range of Silicon Photonic Structures. In Proceedings of the 2007 Photonics in Switching; August 2007; pp. 67–68.
69. Zhang, S.; Zhai, T.; Cui, L.; Shi, X.; Ge, K.; Liang, N.; Hayat, A. Tunable WGM Laser Based on the Polymer Thermo-Optic Effect. *Polymers* **2021**, *13*, 205, doi:10.3390/polym13020205.
70. Zhang, X.; Deng, G.; Yang, H.; Shen, L.; Zhu, Y.; Zhou, S. Electrical Thermo-Optic Tuning of Ultrahigh-Q Silica Microsphere with Laser-Induced Graphene. *Optics Communications* **2023**, *536*, 129371, doi:10.1016/j.optcom.2023.129371.
71. Yin, Y.; Yao, M.; Ding, Y.; Xu, X.; Li, Y.; Wu, Y.; Zhang, D. Polymer/Silica Hybrid Waveguide Thermo-Optic VOA Covering O-Band. *Micromachines* **2022**, *13*, 511, doi:10.3390/mi13040511.
72. Guo, P.; Sarangan, A.M.; Agha, I. A Review of Germanium-Antimony-Telluride Phase Change Materials for Non-Volatile Memories and Optical Modulators. *Applied Sciences* **2019**, *9*, 530, doi:10.3390/app9030530.
73. Nejadriahi, H.; Friedman, A.; Sharma, R.; Pappert, S.; Fainman, Y.; Yu, P. Thermo-Optic Properties of Silicon-Rich Silicon Nitride for on-Chip Applications. *Opt. Express, OE* **2020**, *28*, 24951–24960, doi:10.1364/OE.396969.
74. Rao, S.; Mallemace, E.D.; Cocorullo, G.; Faggio, G.; Messina, G.; Della Corte, F.G. Temperature Dependence of the Thermo-Optic Coefficient in 4H-SiC and GaN Slabs at the Wavelength of 1550 Nm. *Sci Rep* **2022**, *12*, 4809, doi:10.1038/s41598-022-08232-x.
75. Helis, D.L.; Melchiorre, A.; Puiu, A.; Benato, G.; Carniti, P.; Continenza, A.; Di Marco, N.; Ferella, A.; Ferrari, C.; Giannessi, F.; et al. First Measurement of Gallium Arsenide as a Low-Temperature Calorimeter. *Eur. Phys. J. C* **2024**, *84*, 749, doi:10.1140/epjc/s10052-024-13123-8.
76. Xu, Z.; Dai, S.; Liu, C.; Wu, Z.; Xu, L. Investigation of the Ga-Sb-S Chalcogenide Glass with Low Thermo-Optic Coefficient as an Acousto-Optic Material. *Ceramics International* **2022**, *48*, 21663–21670, doi:10.1016/j.ceramint.2022.04.144.
77. Maeder, A.; Kaufmann, F.; Pohl, D.; Kellner, J.; Grange, R. High-Bandwidth Thermo-Optic Phase Shifters for Lithium Niobate-on-Insulator Photonic Integrated Circuits. *Opt. Lett., OL* **2022**, *47*, 4375–4378, doi:10.1364/OL.469358.
78. Sun, L.; Li, X.; Hu, P.; Wang, H.; Zhang, Y.; Tang, G.; He, X.; Dong, J.; Su, Y. Thermally Tunable Add-Drop Filter Based on Valley Photonic Crystals for Optical Communications. *Nanophotonics* **2024**, *13*, 4459–4470, doi:10.1515/nanoph-2024-0437.
79. Dai, D.; Chen, S.; Yu, L.; Shi, Y. Thermally Switchable/Tunable Photonic Integrated Devices on Silicon. In Proceedings of the 2016 Progress in Electromagnetic Research Symposium (PIERS); August 2016; pp. 2359–2359.

 doi:10.20944/preprints202505.0911.v1

80. Tong, W.; Li, S.; Zhang, J.; Dong, J.; Hu, B.; Zhang, X. Thermo-Optic Switch with High Tuning Efficiency Based on Nanobeam Cavity and Hydrogen-Doped Indium Oxide Microheater. *Photonics* **2024**, *11*, 738, doi:10.3390/photonics11080738.
81. Hamze, A.K.; Reynaud, M.; Geler-Kremer, J.; Demkov, A.A. Design Rules for Strong Electro-Optic Materials. *npj Comput Mater* **2020**, *6*, 1–9, doi:10.1038/s41524-020-00399-z.
82. Walker, R.G.; O'Keefe, M.F.; Cameron, N.; Ereifej, H.; Brast, T. Gallium Arsenide Electro-Optic Modulators. In Proceedings of the 2014 IEEE Compound Semiconductor Integrated Circuit Symposium (CSICS); October 2014; pp. 1–4.
83. Stepanenko, M.; Yunusov, I.; Arykov, V.; Troyan, P.; Zhidik, Y. Multi-Parameter Optimization of an InP Electro-Optic Modulator. *Symmetry* **2020**, *12*, 1920, doi:10.3390/sym12111920.
84. Ullah, F.; Deng, N.; Qiu, F. Recent Progress in Electro-Optic Polymer for Ultra-Fast Communication. *PhotoniX* **2021**, *2*, 13, doi:10.1186/s43074-021-00036-y.
85. Brimont, A.; Thomson, D.J.; Sanchis, P.; Herrera, J.; Gardes, F.Y.; Fedeli, J.M.; Reed, G.T.; Martí, J. High Speed Silicon Electro-Optical Modulators Enhanced via Slow Light Propagation. *Opt. Express, OE* **2011**, *19*, 20876–20885, doi:10.1364/OE.19.020876.
86. Zhang, Y.; Shen, J.; Li, J.; Wang, H.; Feng, C.; Zhang, L.; Sun, L.; Xu, J.; Liu, M.; Wang, Y.; et al. High-Speed Electro-Optic Modulation in Topological Interface States of a One-Dimensional Lattice. *Light Sci Appl* **2023**, *12*, 206, doi:10.1038/s41377-023-01251-x.
87. Rabiei, P.; Ma, J.; Khan, S.; Chiles, J.; Fathpour, S. Heterogeneous Lithium Niobate Photonics on Silicon Substrates. *Opt. Express, OE* **2013**, *21*, 25573–25581, doi:10.1364/OE.21.025573.
88. Song, L.; Liu, W.; Guo, Z.; Zhao, S.; Li, H.; Dai, D.; Shi, Y. High-Performance Thin-Film Lithium Niobate Optical 90° Hybrid with a Novel CMRR Assessment Method. *Optics & Laser Technology* **2024**, *179*, 111315, doi:10.1016/j.optlastec.2024.111315.
89. Zhang, F.; Su, Z.; Li, Z.; Zhu, Y.; Gagrani, N.; Li, Z.; Lockrey, M.; Li, L.; Aharonovich, I.; Lu, Y.; et al. High-Speed Multiwavelength InGaAs/InP Quantum Well Nanowire Array Micro-LEDs for next Generation Optical Communications. *OES* **2023**, *2*, 230003–230011, doi:10.29026/oes.2023.230003.
90. Karvounis, A.; Timpu, F.; Vogler-Neuling, V.V.; Savo, R.; Grange, R. Barium Titanate Nanostructures and Thin Films for Photonics. *Advanced Optical Materials* **2020**, *8*, 2001249, doi:10.1002/adom.202001249.
91. Karvounis, A.; Timpu, F.; Vogler-Neuling, V.V.; Savo, R.; Grange, R. Barium Titanate Nanostructures and Thin Films for Photonics. *Advanced Optical Materials* **2020**, *8*, 2001249, doi:10.1002/adom.202001249.
92. Vyas, K.; Espinosa, D.H.G.; Hutama, D.; Jain, S.K.; Mahjoub, R.; Mobini, E.; Awan, K.M.; Lundeen, J.; Dolgaleva, K. Group III-V Semiconductors as Promising Nonlinear Integrated Photonic Platforms. *Advances in Physics: X* **2022**, *7*, 2097020, doi:10.1080/23746149.2022.2097020.
93. Benea-Chelmus, I.-C.; Mason, S.; Meretska, M.L.; Elder, D.L.; Kazakov, D.; Shams-Ansari, A.; Dalton, L.R.; Capasso, F. Gigahertz Free-Space Electro-Optic Modulators Based on Mie Resonances. *Nat Commun* **2022**, *13*, 3170, doi:10.1038/s41467-022-30451-z.
94. Li, J.; Yao, H.; Deng, J.; Hu, Z.; Zhao, Z.; Ma, X.; Chen, K. Electro-Optic Tunable Optical Filter Based on Long-Period Waveguide Grating in Lithium Niobate on Insulator with Absorption Ribbons. *Opt. Express, OE* **2023**, *31*, 30658–30668, doi:10.1364/OE.501813.
95. Butt, M.A. A Perspective on Plasmonic Metasurfaces: Unlocking New Horizons for Sensing Applications. *Nanotechnology* **2025**, *36*, 182501, doi:10.1088/1361-6528/adc30f.
96. Arsenault, R.; Gregoris, D.; Woolven, S.; Ristic, V.M. Waveguide Propagation-Loss Measurement Technique. *Opt. Lett., OL* **1987**, *12*, 1047–1049, doi:10.1364/OL.12.001047.
97. Baehr-Jones, T.; Spott, A.; Ilic, R.; Spott, A.; Penkov, B.; Asher, W.; Hochberg, M. Silicon-on-Sapphire Integrated Waveguides for the Mid-Infrared. *Opt. Express, OE* **2010**, *18*, 12127–12135, doi:10.1364/OE.18.012127.
98. Wang, S.; Tu, Z.; Liu, Y.; Li, X.; Song, R.; Li, Z.; Yue, W.; Cai, Y.; Yu, M. High-Speed Mid-Infrared Silicon-Based Electro-Optic Modulator at 2 Mm. *Optics Communications* **2024**, *565*, 130657, doi:10.1016/j.optcom.2024.130657.

 doi:10.20944/preprints202505.0911.v1

99. Sabatti, A.; Kellner, J.; Kaufmann, F.; Chapman, R.J.; Finco, G.; Kuttner, T.; Maeder, A.; Grange, R. Extremely High Extinction Ratio Electro-Optic Modulator via Frequency Upconversion to Visible Wavelengths. *Opt. Lett., OL* **2024**, *49*, 3870–3873, doi:10.1364/OL.525733.
100. Hsieh, Y.-D.; Lin, J.-H.; Soref, R.; Sun, G.; Cheng, H.-H.; Chang, G.-E. Electro-Absorption Modulation in GeSn Alloys for Wide-Spectrum Mid-Infrared Applications. *Commun Mater* **2021**, *2*, 1–8, doi:10.1038/s43246-021-00144-z.
101. George, J.K.; Mehrabian, A.; Amin, R.; Meng, J.; Lima, T.F. de; Tait, A.N.; Shastri, B.J.; El-Ghazawi, T.; Prucnal, P.R.; Sorger, V.J. Neuromorphic Photonics with Electro-Absorption Modulators. *Opt. Express, OE* **2019**, *27*, 5181–5191, doi:10.1364/OE.27.005181.
102. Zhou, D.; Liang, S.; Zhang, R.; Yang, Q.; Zhu, X.; Lu, D.; Zhao, L.; Wang, W. 50 Gb/s Electro-Absorption Modulator Integrated with a Distributed Feedback Laser for Passive Optical Network Systems. *Photonics* **2022**, *9*, 780, doi:10.3390/photonics9100780.
103. Hong, J.; Qiu, F.; Cheng, X.; Spring, A.M.; Yokoyama, S. A High-Speed Electro-Optic Triple-Microring Resonator Modulator. *Sci Rep* **2017**, *7*, 4682, doi:10.1038/s41598-017-04851-x.
104. Qiu, F.; Han, Y. Electro-Optic Polymer Ring Resonator Modulators [Invited]. *Chin. Opt. Lett., COL* **2021**, *19*, 041301.
105. Chen, X.; Lin, J.; Wang, K. A Review of Silicon-Based Integrated Optical Switches. *Laser & Photonics Reviews* **2023**, *17*, 2200571, doi:10.1002/lpor.202200571.
106. Zhou, L.; Lu, L.; Zhao, S.; Guo, Z.; Li, D.; Chen, J. Large-Scale Silicon Photonic Switches Using Electro-Optic MZIs. In Proceedings of the Optical Fiber Communication Conference (2017), paper W4E.1; Optica Publishing Group, March 19 2017; p. W4E.1.
107. Li, J.; Li, Y.; Meng, Q.; Zhou, Z.; Jia, D.; McIntosh, R.; Bhalla, A.S.; Guo, R. Large Electro-Optic Response of Bulk Ferroelectric Crystals Enhanced by Piezoelectric Resonance in the High Frequency Range. *Materials Research Bulletin* **2018**, *97*, 523–529, doi:10.1016/j.materresbull.2017.09.020.
108. Hou, S.; Hu, H.; Liu, Z.; Xing, W.; Zhang, J.; Hao, Y. High-Speed Electro-Optic Modulators Based on Thin-Film Lithium Niobate. *Nanomaterials* **2024**, *14*, 867, doi:10.3390/nano14100867.
109. Vasudevan, A.T.; Vura, S.; Molleti, S.H.; Nukala, P.; Raghavan, S.; Selvaraja, S.K. Thin-Film Ferroelectric Material Qualification for on-Chip Electro-Optic Applications. In Proceedings of the CLEO 2024 (2024), paper JTh2A.7; Optica Publishing Group, May 5 2024; p. JTh2A.7.
110. Wang, D.Y.; Li, S.; Chan, H.L.W.; Choy, C.L. Electro-Optic Characterization of Epitaxial Ba0.7Sr0.3TiO3 Thin Films Using Prism Coupling Technique. *Current Applied Physics* **2011**, *11*, S52–S55, doi:10.1016/j.cap.2010.09.014.
111. Cullen, C.J.; Murakowski, J.; Shi, S.; Prather, D.W. Thin-Film Silicon Nitride on Electro-Optic Materials for a Novel Modulator Architecture. In Proceedings of the 2018 IEEE Research and Applications of Photonics In Defense Conference (RAPID); August 2018; pp. 1–4.
112. Wang, M.; Chen, Y.; Zhang, S.; Dong, L.; Yao, H.; Xu, H.; Chen, K.; Wu, J. Perspectives of Thin-Film Lithium Niobate and Electro-Optic Polymers for High-Performance Electro-Optic Modulation. *J. Mater. Chem. C* **2023**, *11*, 11107–11122, doi:10.1039/D3TC01132A.
113. Christensen, A.; Reynaud, M.; Posadas, A.B.; Zhan, X.; Warner, J.H.; Demkov, A.A. Electro-Optic Effect in Thin Film Strontium Barium Niobate (SBN) Grown by RF Magnetron Sputtering on SrTiO3 Substrates. *Journal of Applied Physics* **2024**, *136*, 013102, doi:10.1063/5.0206229.
114. Tao, J.; Yang, Y.; Li, X.; Wang, P.; Li, J.; Liu, J. Broadband Thin-Film Lithium Niobate Electro-Optic Modulator. *Photonics* **2024**, *11*, 325, doi:10.3390/photonics11040325.
115. Ranno, L.; Sia, J.X.B.; Dao, K.P.; Hu, J. Multi-Material Heterogeneous Integration on a 3-D Photonic-CMOS Platform. *Opt. Mater. Express, OME* **2023**, *13*, 2711–2725, doi:10.1364/OME.497245.
116. Li, H.; Wang, Z.; Lu, Q.; Wang, L.; Tan, Y.; Chen, F. Heterogeneous Integration of an On-Chip Nd:YAG Whispering Gallery Mode Laser with a Lithium-Niobate-on-Insulator Platform. *Opt. Lett., OL* **2024**, *49*, 1397–1400, doi:10.1364/OL.515441.
117. Kaur, P.; Boes, A.; Ren, G.; Nguyen, T.G.; Roelkens, G.; Mitchell, A. Hybrid and Heterogeneous Photonic Integration. *APL Photonics* **2021**, *6*, 061102, doi:10.1063/5.0052700.

 doi:10.20944/preprints202505.0911.v1

118. Matsumoto, A.; Yamamoto, N. Advanced Monolithic and Heterogeneous Photonic Integration Technology. In *Handbook of Radio and Optical Networks Convergence*; Kawanishi, T., Ed.; Springer Nature: Singapore, 2023; pp. 1–34 ISBN 978-981-334-999-5.
119. Ranno, L.; Sia, J.X.B.; Dao, K.P.; Hu, J. Heterogeneous Integration of Active Photonic Materials Leveraging Substrate-Inverted Multimaterial Integration Technology (SuMMIT). In Proceedings of the Active Photonic Platforms (APP) 2024; SPIE, October 2 2024; Vol. 13110, pp. 48–56.
120. Komljenovic, T.; Huang, D.; Pintus, P.; Tran, M.A.; Davenport, M.L.; Bowers, J.E. Photonic Integrated Circuits Using Heterogeneous Integration on Silicon. *Proceedings of the IEEE* **2018**, *106*, 2246–2257, doi:10.1109/JPROC.2018.2864668.
121. Li, Z.; Chen, Y.; Wang, S.; Xu, F.; Xu, Q.; Zhang, J.; Zhu, Q.; Yue, W.; Ou, X.; Cai, Y.; et al. Lithium Niobate Electro-Optical Modulator Based on Ion-Cut Wafer Scale Heterogeneous Bonding on Patterned SOI Wafers. *Photon. Res., PRJ* **2025**, *13*, 106–112, doi:10.1364/PRJ.534954.
122. Li, Q.; Zhu, H.; Zhang, H.; Cai, L.; Hu, H. Phase Modulators in Hybrid Silicon and Lithium Niobate Thin Films. *Opt. Mater. Express, OME* **2022**, *12*, 1314–1322, doi:10.1364/OME.452404.
123. Lin, Q.; Huang, J.; Xue, Y.; Lin, L.; Xing, Z.; Wong, K.S.; Lau, K.M. GaAs Microdisk Lasers with Al2O3 Passivation Selectively Grown on SOI. *ACS Photonics* **2024**, *11*, 3578–3584, doi:10.1021/acsphotonics.4c00527.
124. Wei, W.-Q.; Feng, Q.; Guo, J.-J.; Guo, M.-C.; Wang, J.-H.; Wang, Z.-H.; Wang, T.; Zhang, J.-J. InAs/GaAs Quantum Dot Narrow Ridge Lasers Epitaxially Grown on SOI Substrates for Silicon Photonic Integration. *Opt. Express, OE* **2020**, *28*, 26555–26563, doi:10.1364/OE.402174.
125. Yan, Z.; Han, Y.; Lin, L.; Xue, Y.; Ma, C.; Ng, W.K.; Wong, K.S.; Lau, K.M. A Monolithic InP/SOI Platform for Integrated Photonics. *Light Sci Appl* **2021**, *10*, 200, doi:10.1038/s41377-021-00636-0.
126. Yan, Z.; Han, Y.; Lin, L.; Xue, Y.; Ma, C.; Ng, W.K.; Sing Wong, K.; Lau, K.M. Lasers on an InP/SOI Platform with Dislocation-Free in-Plane InP Sub-Micron Bars and Membranes. In Proceedings of the 2021 27th International Semiconductor Laser Conference (ISLC); October 2021; pp. 1–2.
127. Han, Y.; Wang, J.; Wan, H.; Wang, S.; Hu, H.; Xiao, T.-H.; Cheng, Z.; Liu, T. Solution Processable Transition Metal Dichalcogenides-Based Hybrids for Photodetection. *Nano Materials Science* **2019**, *1*, 288–298, doi:10.1016/j.nanoms.2019.09.010.
128. Fu, Q.; Han, J.; Wang, X.; Xu, P.; Yao, T.; Zhong, J.; Zhong, W.; Liu, S.; Gao, T.; Zhang, Z.; et al. 2D Transition Metal Dichalcogenides: Design, Modulation, and Challenges in Electrocatalysis. *Advanced Materials* **2021**, *33*, 1907818, doi:10.1002/adma.201907818.
129. Fan, Z.; Geng, Z.; Fang, W.; Lv, X.; Su, Y.; Wang, S.; Liu, J.; Chen, H. Characteristics of Transition Metal Dichalcogenides in Optical Pumped Modulator of Terahertz Wave. *AIP Advances* **2020**, *10*, 045304, doi:10.1063/1.5141511.
130. Isichenko, A.; Hunter, A.S.; Bose, D.; Chauhan, N.; Song, M.; Liu, K.; Harrington, M.W.; Blumenthal, D.J. Sub-Hz Fundamental, Sub-kHz Integral Linewidth Self-Injection Locked 780 Nm Hybrid Integrated Laser. *Sci Rep* **2024**, *14*, 27015, doi:10.1038/s41598-024-76699-x.
131. Butt, M.A. Insight into Plasmonics: Resurrection of Modern-Day Science (Invited). *Computer Optics 48*, 5–17.
132. Barbillon, G. Plasmonics and Its Applications. *Materials* **2019**, *12*, 1502, doi:10.3390/ma12091502.
133. Butt, M.A. Plasmonic Sensor System Embedded with Orthogonal Mode Couplers for Simultaneous Monitoring of Temperature and Refractive Index. *Plasmonics* **2024**, doi:10.1007/s11468-024-02303-7.
134. Mcoyi, M.P.; Mpofu, K.T.; Sekhwama, M.; Mthunzi-Kufa, P. Developments in Localized Surface Plasmon Resonance. *Plasmonics* **2024**, doi:10.1007/s11468-024-02620-x.
135. Hu, X.; Lu, C.; Zhao, X.; Gu, Y.; Lu, M.; Sun, D. A Multi-Parameter Tunable Plasmon Modulator. *Sci Rep* **2023**, *13*, 11483, doi:10.1038/s41598-023-38799-y.
136. Butt, M.A.; Kazansky, N.L. Narrowband Perfect Metasurface Absorber Based on Impedance Matching. *Photonics Letters of Poland* **2020**, *12*, 88–90, doi:10.4302/plp.v12i3.1041.
137. Ding, F.; Meng, C.; Bozhevolnyi, S.I. Electrically Tunable Optical Metasurfaces. *Photonics Insights* **2024**, *3*, R07, doi:10.3788/PI.2024.R07.
138. Kazanskiy, N.L.; Khonina, S.N.; Butt, M.A. Metasurfaces: Shaping the Future of Photonics. *Science Bulletin* **2024**, doi:10.1016/j.scib.2024.04.056.

 doi:10.20944/preprints202505.0911.v1

139. Badloe, T.; Lee, J.; Seong, J.; Rho, J. Tunable Metasurfaces: The Path to Fully Active Nanophotonics. *Advanced Photonics Research* **2021**, *2*, 2000205.
140. Kim, J.; Seong, J.; Yang, Y.; Moon, S.-W.; Badloe, T.; Rho, J. Tunable Metasurfaces towards Versatile Metalenses and Metaholograms: A Review. *AP* **2022**, *4*, 024001, doi:10.1117/1.AP.4.2.024001.
141. Zhang, J.; Kosugi, Y.; Ogasawara, M.; Ariu, K.; Otomo, A.; Yamada, T.; Nakano, Y.; Tanemura, T. High-Speed Metasurface Modulator Using Perfectly Absorptive Bimodal Plasmonic Resonance. *APL Photonics* **2023**, *8*, 121304, doi:10.1063/5.0173216.
142. Xie, Y.; McDonald, C.A.; Morin, T.J.; Zhou, Z.; Peters, J.; Bowers, J.E.; Wan, Y. High-Efficiency Tunable Lasers Hybrid-Integrated with Silicon Photonics at 2.0 μm. *Photon. Res., PRJ* **2025**, *13*, 737–742, doi:10.1364/PRJ.550770.
143. Liu, L.; Liao, S.; Xue, W.; Yue, J. Tunable All-Optical Microwave Filter with High Tuning Efficiency. *Opt. Express, OE* **2020**, *28*, 6918–6928, doi:10.1364/OE.384823.
144. Chen, Y.; Whitehead, J.; Ryou, A.; Zheng, J.; Xu, P.; Fryett, T.; Majumdar, A. Large Thermal Tuning of a Polymer-Embedded Silicon Nitride Nanobeam Cavity. *Opt. Lett., OL* **2019**, *44*, 3058–3061, doi:10.1364/OL.44.003058.
145. Li, Z.; Wang, Y.; Wu, J.; Wang, Z.; Lou, M.; Sun, K.; Qiu, J.; Tan, D. Mode-Tunable Low-Loss Waveguides in Glass for Visible Light Photonic Integrated Devices. *Optics and Lasers in Engineering* **2024**, *182*, 108467, doi:10.1016/j.optlaseng.2024.108467.
146. Rasras, M.S.; Tu, K.-Y.; Gill, D.M.; Chen, Y.-K.; White, A.E.; Patel, S.S.; Pomerene, A.; Carothers, D.; Beattie, J.; Beals, M.; et al. Demonstration of a Tunable Microwave-Photonic Notch Filter Using Low-Loss Silicon Ring Resonators. *J. Lightwave Technol., JLT* **2009**, *27*, 2105–2110.
147. Pruessner, M.W.; Tyndall, N.F.; Walsh, K.J.; Stievater, T.H. Enhanced Thermo-Optic Effects in Silicon Nitride Photonic Integrated Circuits via Polymer Claddings. *JNP* **2023**, *17*, 046001, doi:10.1117/1.JNP.17.046001.
148. Malik, A.; Dwivedi, S.; Landschoot, L.V.; Muneeb, M.; Shimura, Y.; Lepage, G.; Campenhout, J.V.; Vanherle, W.; Opstal, T.V.; Loo, R.; et al. Ge-on-Si and Ge-on-SOI Thermo-Optic Phase Shifters for the Mid-Infrared. *Opt. Express, OE* **2014**, *22*, 28479–28488, doi:10.1364/OE.22.028479.
149. Parra, J.; Hurtado, J.; Griol, A.; Sanchis, P. Ultra-Low Loss Hybrid ITO/Si Thermo-Optic Phase Shifter with Optimized Power Consumption. *Opt. Express, OE* **2020**, *28*, 9393–9404, doi:10.1364/OE.386959.
150. Jiang, X.; Wu, J.; Yang, Y.; Pan, T.; Mao, J.; Liu, B.; Liu, R.; Zhang, Y.; Qiu, C.; Tremblay, C.; et al. Wavelength and Bandwidth-Tunable Silicon Comb Filter Based on Sagnac Loop Mirrors with Mach-Zehnder Interferometer Couplers. *Opt. Express, OE* **2016**, *24*, 2183–2188, doi:10.1364/OE.24.002183.
151. Zheng, S.; Zhou, N.; Long, Y.; Ruan, Z.; Du, J.; Hu, X.; Shen, L.; Li, S.; Wang, J. Compact Tunable Photonic Comb Filter on a Silicon Platform. *Opt. Lett., OL* **2017**, *42*, 2762–2765, doi:10.1364/OL.42.002762.
152. Wang, H.; Dai, J.; Jia, H.; Shao, S.; Fu, X.; Zhang, L.; Yang, L. Polarization-Independent Tunable Optical Filter with Variable Bandwidth Based on Silicon-on-Insulator Waveguides. *Nanophotonics* **2018**, *7*, 1469–1477, doi:10.1515/nanoph-2018-0058.
153. St-Yves, J.; Bahrami, H.; Jean, P.; LaRochelle, S.; Shi, W. Widely Bandwidth-Tunable Silicon Filter with an Unlimited Free-Spectral Range. *Opt. Lett., OL* **2015**, *40*, 5471–5474, doi:10.1364/OL.40.005471.
154. Singh, N.; Lorenzen, J.; Kilinc, M.; Wang, K.; Sinobad, M.; Francis, H.; Carreira, J.; Geiselmann, M.; Demirbas, U.; Pergament, M.; et al. Sub-2W Tunable Laser Based on Silicon Photonics Power Amplifier. *Light Sci Appl* **2025**, *14*, 18, doi:10.1038/s41377-024-01681-1.
155. Daudlin, S.; Rizzo, A.; Lee, S.; Khilwani, D.; Ou, C.; Wang, S.; Novick, A.; Gopal, V.; Cullen, M.; Parsons, R.; et al. Three-Dimensional Photonic Integration for Ultra-Low-Energy, High-Bandwidth Interchip Data Links. *Nat. Photon.* **2025**, 1–8, doi:10.1038/s41566-025-01633-0.
156. Malik, A.; Liu, S.; Timurdogan, E.; Harrington, M.; Netherton, A.; Saeidi, M.; Blumenthal, D.J.; Theogarajan, L.; Watts, M.; Bowers, J.E. Low Power Consumption Silicon Photonics Datacenter Interconnects Enabled by a Parallel Architecture. In Proceedings of the 2021 Optical Fiber Communications Conference and Exhibition (OFC); June 2021; pp. 1–3.
157. Zhou, Z.; Yin, B.; Deng, Q.; Li, X.; Cui, J. Lowering the Energy Consumption in Silicon Photonic Devices and Systems [Invited]. *Photon. Res., PRJ* **2015**, *3*, B28–B46, doi:10.1364/PRJ.3.000B28.

 doi:10.20944/preprints202505.0911.v1

158. Zhong, H.; Li, J.; He, Y.; Zhang, R.; Wang, H.; Shen, J.; Zhang, Y.; Su, Y. Ultra-Low-Power Consumption Silicon Electro-Optic Switch Based on Photonic Crystal Nanobeam Cavity. *npj Nanophoton.* **2024**, *1*, 1–7, doi:10.1038/s44310-024-00032-7.
159. Miura, H.; Qiu, F.; Spring, A.M.; Kashino, T.; Kikuchi, T.; Ozawa, M.; Nawata, H.; Odoi, K.; Yokoyama, S. High Thermal Stability 40 GHz Electro-Optic Polymer Modulators. *Opt. Express, OE* **2017**, *25*, 28643–28649, doi:10.1364/OE.25.028643.
160. Agarwal, S.; Mishra, J.K.; Priye, V. Thermal Design Management of Highly Mechanically Stable Wavelength Shifter Using Photonic Crystal Waveguide. *Superlattices and Microstructures* **2020**, *142*, 106510, doi:10.1016/j.spmi.2020.106510.
161. Zeng, Z.; Zhang, Z.; Zhang, L.; Zhang, S.; Zhang, Y.; Sun, B.; Liu, Y. Stable and Finely Tunable Optoelectronic Oscillator Based on Stimulated Brillouin Scattering and an Electro-Optic Frequency Shift. *Appl. Opt., AO* **2020**, *59*, 589–594, doi:10.1364/AO.378196.
162. Kieninger, C.; Kutuvantavida, Y.; Miura, H.; Kemal, J.N.; Zwickel, H.; Qiu, F.; Lauermann, M.; Freude, W.; Randel, S.; Yokoyama, S.; et al. Demonstration of Long-Term Thermally Stable Silicon-Organic Hybrid Modulators at 85 °C. *Opt. Express, OE* **2018**, *26*, 27955–27964, doi:10.1364/OE.26.027955.
163. Gardes, F.; Shooa, A.; De Paoli, G.; Skandalos, I.; Ilie, S.; Rutirawut, T.; Talataisong, W.; Faneca, J.; Vitali, V.; Hou, Y.; et al. A Review of Capabilities and Scope for Hybrid Integration Offered by Silicon-Nitride-Based Photonic Integrated Circuits. *Sensors* **2022**, *22*, 4227, doi:10.3390/s22114227.
164. Shahbaz, M.; Butt, M.A.; Piramidowicz, R. Breakthrough in Silicon Photonics Technology in Telecommunications, Biosensing, and Gas Sensing. *Micromachines* **2023**, *14*, 1637, doi:10.3390/mi14081637.
165. Churaev, M.; Wang, R.N.; Riedhauser, A.; Snigirev, V.; Blésin, T.; Möhl, C.; Anderson, M.H.; Siddharth, A.; Popoff, Y.; Drechsler, U.; et al. A Heterogeneously Integrated Lithium Niobate-on-Silicon Nitride Photonic Platform. *Nat Commun* **2023**, *14*, 3499, doi:10.1038/s41467-023-39047-7.
166. Dong, Z.; Raju, A.; Posadas, A.B.; Reynaud, M.; Demkov, A.A.; Wasserman, D.M. Monolithic Barium Titanate Modulators on Silicon-on-Insulator Substrates. *ACS Photonics* **2023**, *10*, 4367–4376, doi:10.1021/acsphotonics.3c01144.
167. Kordlar, A.G.; Koohsorkhi, J.; Nejad, E.T. Barium Titanate Nanorods on Micro-Machined Silicon Substrate for Performance Enhancement of Piezoelectric Nanogenerators (NGs). *Solid-State Electronics* **2021**, *186*, 108168, doi:10.1016/j.sse.2021.108168.
168. Schulz, K.M.; Prorok, S.; Jalas, D.; Marder, S.R.; Luo, J.; Jen, A.K.-Y.; Zierold, R.; Nielsch, K.; Eich, M. Mechanism That Governs the Electro-Optic Response of Second-Order Nonlinear Polymers on Silicon Substrates. *Opt. Mater. Express, OME* **2015**, *5*, 1653–1660, doi:10.1364/OME.5.001653.
169. Taghavi, I.; Moridsadat, M.; Tofini, A.; Raza, S.; Jaeger, N.A.F.; Chrostowski, L.; Shastri, B.J.; Shekhar, S. Polymer Modulators in Silicon Photonics: Review and Projections. *Nanophotonics* **2022**, *11*, 3855–3871, doi:10.1515/nanoph-2022-0141.
170. Artel, V.; Ilovitsh, T.; Bakish, I.; Shubely, M.; Shekel, E.; Ben-Ezra, Y.; Sukenik, C.N.; Zadok, A. Wafer Bonding Techniques for Hybrid Silicon Photonic Devices Based on Surface Modifications. In Proceedings of the 2012 14th International Conference on Transparent Optical Networks (ICTON); July 2012; pp. 1–4.
171. Du, C.; Zhao, Y.; Li, Y. Effect of Surface Cleaning Process on the Wafer Bonding of Silicon and Pyrex Glass. *J Inorg Organomet Polym* **2023**, *33*, 673–679, doi:10.1007/s10904-022-02510-x.
172. M.A. Butt Thin-Film Coating Methods: A Successful Marriage of High-Quality and Cost-Effectiveness—A Brief Exploration. *Coatings* **2022**, *12*, 1115.
173. Allouti, N.; Chevalier, P.; Bérard-Bergery, S.; Rousset, V.; Mortini, B.; Quéméré, P.; Tomaso, F.; Coquand, R. Grayscale Lithography Process Study for Sub 5µm Microlens Patterns. In Proceedings of the Novel Patterning Technologies for Semiconductors, MEMS/NEMS, and MOEMS 2019; SPIE, March 26 2019; Vol. 10958, pp. 16–30.
174. Qin, D.; Xia, Y.; Whitesides, G.M. Soft Lithography for Micro- and Nanoscale Patterning. *Nat Protoc* **2010**, *5*, 491–502, doi:10.1038/nprot.2009.234.
175. Sreekanth, K.V.; Chua, J.K.; Murukeshan, V.M. Interferometric Lithography for Nanoscale Feature Patterning: A Comparative Analysis between Laser Interference, Evanescent Wave Interference, and Surface Plasmon Interference. *Appl. Opt., AO* **2010**, *49*, 6710–6717, doi:10.1364/AO.49.006710.

 doi:10.20944/preprints202505.0911.v1

176. Zhu, C.; Bamidele, E.A.; Shen, X.; Zhu, G.; Li, B. Machine Learning Aided Design and Optimization of Thermal Metamaterials. *Chem. Rev.* **2024**, *124*, 4258–4331, doi:10.1021/acs.chemrev.3c00708.
177. Cetinkaya, C.; Cokduygulular, E.; Aykut, M.Y.; Erkal, O.; Aydogmus, F.; Kinaci, B. Artificial Intelligence-Empowered Functional Design of Semi-Transparent Optoelectronic and Photonic Devices via Deep Q-Learning. *Sci Rep* **2025**, *15*, 13508, doi:10.1038/s41598-025-94586-x.
178. Jin, Z.; Mei, S.; Chen, S.; Li, Y.; Zhang, C.; He, Y.; Yu, X.; Yu, C.; Yang, J.K.W.; Luk'yanchuk, B.; et al. Complex Inverse Design of Meta-Optics by Segmented Hierarchical Evolutionary Algorithm. *ACS Nano* **2019**, *13*, 821–829, doi:10.1021/acsnano.8b08333.
179. Butt, M.A.; Mateos, X. Strategic Insights into Integrated Photonics: Core Concepts, Practical Deployments, and Future Outlook. *Applied Sciences* **2024**, *14*, 6365, doi:10.3390/app14146365.
180. Butt, M.A.; Mateos, X.; Piramidowicz, R. Photonics Sensors: A Perspective on Current Advancements, Emerging Challenges, and Potential Solutions (Invited). *Physics Letters A* **2024**, *516*, 129633, doi:10.1016/j.physleta.2024.129633.
181. Lebedev, V.A.; Amer, A.E. Limitations of Using Phase Change Materials for Thermal Energy Storage. *IOP Conf. Ser.: Earth Environ. Sci.* **2019**, *378*, 012044, doi:10.1088/1755-1315/378/1/012044.
182. He, Z.; Tan, G.; Chanda, D.; Wu, S.-T. Novel Liquid Crystal Photonic Devices Enabled by Two-Photon Polymerization [Invited]. *Opt. Express, OE* **2019**, *27*, 11472–11491, doi:10.1364/OE.27.011472.
183. Judeinstein, P.; Sanchez, C. Hybrid Organic–Inorganic Materials: A Land of Multidisciplinarity. *J. Mater. Chem.* **1996**, *6*, 511–525, doi:10.1039/JM9960600511.
184. Zhao, X.; Du, Y.; Li, W.; Zhao, Z.; Lei, M. Organic/Inorganic Hybrids for Intelligent Sensing and Wearable Clean Energy Applications. *Adv Compos Hybrid Mater* **2023**, *6*, 176, doi:10.1007/s42114-023-00751-z.
185. Khonina, S.N.; Kazanskiy, N.L.; Butt, M.A. Grayscale Lithography and a Brief Introduction to Other Widely Used Lithographic Methods: A State-of-the-Art Review. *Micromachines* **2024**, *15*, 1321, doi:10.3390/mi15111321.
186. Iftekar, S.F.; Aabid, A.; Amir, A.; Baig, M. Advancements and Limitations in 3D Printing Materials and Technologies: A Critical Review. *Polymers* **2023**, *15*, 2519, doi:10.3390/polym15112519.
187. Chen, J.; Ji, J.; Xie, C.; Wang, Y. Research on the Tunable Optical Alignment Technology of Lidar Under Complex Working Conditions. *Remote Sensing* **2025**, *17*, 532, doi:10.3390/rs17030532.
188. Nath, S.K.; Das, S.K.; Nandi, S.K.; Xi, C.; Marquez, C.V.; Rúa, A.; Uenuma, M.; Wang, Z.; Zhang, S.; Zhu, R.-J.; et al. Optically Tunable Electrical Oscillations in Oxide-Based Memristors for Neuromorphic Computing. *Advanced Materials* **2024**, *36*, 2400904, doi:10.1002/adma.202400904.
189. El Srouji, L.; Krishnan, A.; Ravichandran, R.; Lee, Y.; On, M.; Xiao, X.; Ben Yoo, S.J. Photonic and Optoelectronic Neuromorphic Computing. *APL Photonics* **2022**, *7*, 051101, doi:10.1063/5.0072090.
190. Bogdanov, S.; Shalaginov, M.Y.; Boltasseva, A.; Shalaev, V.M. Material Platforms for Integrated Quantum Photonics. *Opt. Mater. Express, OME* **2017**, *7*, 111–132, doi:10.1364/OME.7.000111.